

Spin-orbit precession for eccentric black hole binaries at first order in the mass ratio

Sarp Akcay,¹ David Dempsey,² and Sam R. Dolan²

¹*School of Mathematical Sciences and Complex & Adaptive Systems Laboratory,
University College Dublin, Belfield, Dublin 4, Ireland.*

²*Consortium for Fundamental Physics, School of Mathematics and Statistics,
University of Sheffield, Hicks Building, Hounsfield Road, Sheffield S3 7RH, United Kingdom.*

(Dated: June 5, 2022)

We consider spin-orbit (“geodetic”) precession for a compact binary in strong-field gravity. Specifically, we compute ψ , the ratio of the accumulated spin-precession and orbital angles over one radial period, for a spinning compact body orbiting a non-rotating black hole. We show that ψ can be computed for eccentric orbits in both the gravitational self-force and post-Newtonian frameworks, and that the results appear to be consistent. We present a post-Newtonian expansion for ψ at next-to-next-to-leading order, and a Lorenz-gauge gravitational self-force calculation for ψ at first order in the mass ratio. The latter provides new numerical data in the strong-field regime to inform the Effective One-Body model of the gravitational two-body problem. We conclude that ψ complements the Detweiler redshift z as a key invariant quantity characterizing eccentric orbits in the gravitational two-body problem.

I. Introduction

The year 2016 will surely come to be regarded as the *annus mirabilis* of gravitational wave astronomy. First, LIGO reported on primogenital detections of gravitational waves (GWs): three distinctive “chirps” associated with the binary black hole mergers GW150914, GW151226 and, at marginal statistical significance, LVT151012 [1–3]. These discoveries suggest that second-generation ground-based detectors, operating at full sensitivity, may detect as many as 1000 black hole mergers per annum [4]. Second, the LISA Pathfinder mission reported on test masses maintained in almost-perfect freefall, with sub-Femto- g accelerations in the relevant frequency band [5]. The path is now clear for eLISA’s launch, circa 2034.

The purpose of a space-based mission such as eLISA [6] is to explore the low-frequency (10^{-4} –1 Hz) gravitational wave sky. Key sources in this band include Extreme Mass-Ratio Inspirals (EMRIs). In a typical EMRI, a compact body of mass $m_1 \sim 1\text{--}10^2 M_\odot$ [in]spirals towards a supermassive black hole of mass $m_2 \sim 10^5\text{--}10^7 M_\odot$ under the influence of radiation reaction [7, 8]. EMRI modelling poses a stiff challenge to Numerical Relativity (NR) [9] due to the separation of scales implied by the mass ratio $q \equiv m_1/m_2 \sim 10^{-3}\text{--}10^{-7}$ (though see e.g. [10]); and to post-Newtonian (pN) theory [11–13], due to the strong-field nature of the orbit.

The gravitational self-force (GSF) programme [14–17], initiated two decades ago [18, 19], seeks to address the EMRI challenge by blending together black hole perturbation theory [20–23], regularization methods [24–28] and certain asymptotic-matching, singular-perturbation and multiple-scale techniques [18, 29–32]. The programme is influenced by some deep-rooted ideas in physics, such as Dirac’s approach to radiation reaction in electromagnetism [33, 34], the effacement principle and effective field theory [35, 36].

The ultimate aim of the GSF programme is to model the orbit (and gravitational waveform) of a typical EMRI, as it evolves over several years through $\sim 10^5$ orbital cycles; without making “slow-motion” or “weak-field” approximations; with a final phase error of less than a radian. Fulfilment of the accuracy goal requires methods for computing dissipative self-force at *next-to-leading-order* in the mass ratio q [37–39]; see Refs. [40–44] for recent progress in this direction.

From one perspective, the compact body m_1 is accelerated away from a geodesic of the background spacetime of m_2 by a GSF, which may be split into a dissipative (“radiation reaction”) and conservative piece with respect to time-reversal. The dissipative self-force at *leading* order in q has been known, in effect, since the 1970s, as it may be deduced from Teukolsky fluxes [22, 45–47]. By contrast, the more subtle consequences of the conservative self-force have only been explored in the last decade. An appealing perspective, offered by Detweiler & Whiting [25] and others [32, 48–50], is that a (non-spinning, non-extended) compact body follows a geodesic in a (fictitious) regularly-perturbed spacetime, $g_{ab}^R = \bar{g}_{ab} + h_{ab}^R$, where \bar{g}_{ab} is the metric of the background spacetime parametrized by m_2 , and $h_{ab}^R = \mathcal{O}(q)$ is a certain smooth vacuum perturbation obtained by subtracting a “singular-symmetric” piece from the physical metric. Conservative GSF effects are manifest as shifts at $\mathcal{O}(q)$ in quantities defined on geodesics.

In 2008, Detweiler [51] showed that, for circular orbits, the $\mathcal{O}(q)$ shift in the redshift invariant $z = (u^t)^{-1} = \frac{dt}{d\tau}$ for circular

orbits (proportional to $h_{uu}^R \equiv h_{ab}^R u^a u^b$, where u^a is the geodesic tangent vector) is independent of the choice of gauge in GSF theory [52], within a helical class. As z is a physical observable (in principle at least), it may be calculated for *any* mass ratio via complementary approaches to the gravitational two-body problem. There has emerged a concordance in results in overlapping domains [53], between GSF theory [51, 52, 54, 55], post-Newtonian theory [51, 56–58], and, most recently, Numerical Relativity [59]. Moreover, the redshift invariant z has been found to play a leading role in the first law of binary black hole mechanics [60–62].

Invariants from GSF theory, such as z , provide strong-field $\mathcal{O}(q)$ information that can be applied to calibrate and enhance the Effective One-Body (EOB) model [63–66]. As the EOB model generates waveforms for binaries at $q \sim 1$, this provides a conduit for GSF results to flow towards data analysis at LIGO. A cottage industry has developed in identifying and calculating invariants associated with conservative GSF at leading order in q . For circular orbits in Schwarzschild, the invariants comprise (i) the redshift invariant [51, 52] (relating also to the binary's binding energy [67]), (ii) the shift in the innermost stable circular orbit (ISCO) [68], (iii) the periapsis advance (of a mildly-eccentric orbit) [68–70], (iv) the geodetic spin-precession invariant [71–75], (v) tidal eigenvalues at quadrupolar order [73, 76, 77], and (vi) tidal invariants at octupolar order [76–78]. There has been remarkable progress in expanding these GSF invariants to very high post-Newtonian orders [75, 79–81].

At present, three tasks are underway. First, the task of computing GSF invariants for a spinning (Kerr) black hole. For circular orbits, (i) the redshift invariant [82, 83] and (ii) the ISCO shift [84] have been calculated; (iii) the periapsis advance has been inferred from NR data [85]; but the higher-order invariants (iv)–(vi) remain to be found. Second, the task of identifying and computing invariants for non-circular geodesics. For eccentric orbits, the redshift is defined by $z = \mathcal{T}/T$, where \mathcal{T} and T are the proper-time and coordinate-time periods for radial motion. The redshift has been computed numerically [69, 86] and also expanded in a pN series [87–89] for eccentric orbits in Schwarzschild. Recently, it was found for equatorial eccentric orbits in Kerr, in [43] and [90], respectively. Yet generalized versions of the higher-order invariants (iv)–(vi) for eccentric equatorial orbits in Schwarzschild have not yet been forthcoming, and generic orbits in Kerr remain an untamed frontier. Third, there remains the ongoing task of transcribing new GSF results into the EOB model [63–66, 76, 88, 91]; and comparing against NR data [59, 70].

In this article, we consider spin-orbit precession for a spinning compact body of mass m_1 on an eccentric orbit about a (perturbed) Schwarzschild black hole of mass m_2 . We focus on the spin-precession scalar ψ , which was defined in the circular-orbit context in Ref. [71] (see also Refs. [72–75]). The natural definition of ψ for eccentric orbits is

$$\psi = \frac{\Phi - \Psi}{\Phi}, \quad (1.1)$$

where Φ and Ψ are, respectively, the orbital angle and the spin-precession angle (with respect to a polar-type basis) accumulated in passing from periapsis to periapsis (i.e. over one radial period). We shall compute $\Delta\psi$, the $\mathcal{O}(m_1)$ contribution to ψ at fixed frequencies, via both GSF and post-Newtonian approaches. In the pN calculation, we work with the spin-orbit Hamiltonian H_{SO} through next-to-next-to-leading-order (NNLO) [92–94], neglecting spin-squared and higher contributions.

The article is organised as follows. In Sec. II we review geodesic motion and spin precession of test-bodies on the Kerr spacetime. In Sec. III we extend the gravitational self-force formalism in order to compute $\Delta\psi$ for eccentric orbits. In Sec. IV we calculate $\Delta\psi$ through NNLO from the spin-orbit Hamiltonian H_{SO} . In Sec. V we present our numerical results, and confront the GSF data with the pN expansion. We conclude in Sec. VI with a discussion of future calculations.

Conventions: We set $G = c = 1$ and use the metric signature +2. Coordinate indices are denoted with Roman letters a, b, c, \dots , indices with respect to a triad are denoted with letters i, j, k, \dots , and general tetrad indices with α, β, \dots , etc., and numerals denote projection onto the tetrad legs. The coordinates (t, r, θ, ϕ) denote general polar coordinates which, on the background Kerr spacetime, correspond to Boyer-Lindquist coordinates. Partial derivatives are denoted with commas, and covariant derivatives with semi-colons, i.e., $k_{a;b} \equiv \nabla_b k_a$. Symmetrization and anti-symmetrization of indices is denoted with round and square brackets, () and [], respectively. Overdots denote derivatives with respect to proper time, i.e. $\dot{r} = \frac{dr}{d\tau}$.

II. GEODESICS AND SPIN PRECESSION IN THE TEST-BODY LIMIT

A. Geodetic spin precession

Let us consider a gyroscope, of inconsequential mass and size, moving along a geodesic $z^a(\tau)$ in a curved spacetime. The geodesic tangent vector $u^a = \frac{dz^a}{d\tau}$ (a unit timelike vector, $g_{ab}u^a u^b = -1$) is parallel-transported, such that $Du^a/d\tau = 0$, where $Dv^a/d\tau \equiv u^b \nabla_b v^a = dv^a/d\tau + \overset{\leftrightarrow}{\Gamma}_{bc}^a u^b v^c$. The gyroscope's spin vector s_a (which is spatial, $s_a u^a = 0$) is parallel-transported along the geodesic, $Ds_a/d\tau = 0$; hence its norm $s^2 \equiv g^{ab} s_a s_b$ is conserved.

We may introduce a reference basis e_α^a (i.e. an orthonormal tetrad) along the geodesic, such that $g_{ab}e_\alpha^a e_\beta^b = \eta_{\alpha\beta}$ where $\eta_{\alpha\beta} = \text{diag}[-1, 1, 1, 1]$ and $e_0^a = u^a$. With this basis, we may recast the parallel-transport equation $Ds_a/d\tau = 0$ in the beguiling form

$$\frac{ds}{d\tau} = \boldsymbol{\omega} \times \mathbf{s}, \quad (2.1)$$

where $(\mathbf{s})_i \equiv e_i^a s_a$, $(\boldsymbol{\omega})_i \equiv -\frac{1}{2}\epsilon_{ijk}\omega^{jk}$, and

$$\omega_{ij} \equiv -g_{ab}e_i^a \frac{De_j^b}{d\tau} = -\omega_{ji}. \quad (2.2)$$

Eq. (2.1) merely describes how a parallel-transported basis varies relative to a reference basis (or ‘body frame’). Note that $\boldsymbol{\omega}$ depends entirely on the choice of reference basis; in particular, if e_i^a is itself parallel-transported, then $\boldsymbol{\omega} = \mathbf{0}$. An obvious way forward, then, is to choose a physically-motivated reference basis. For example, one could choose the eigenvectors of the 3×3 tidal matrix $C_{ij} \equiv C_{abcd}e_i^a u^b e_j^c u^d$, where C_{abcd} is the Weyl tensor. As C_{ij} is real and symmetric, the eigenvectors define a unique orthogonal basis (provided that the eigenvalues are distinct).

Let us suppose that a natural reference basis exists, and furthermore that $\boldsymbol{\omega}$ is fixed in direction (typically, orthogonal to the orbital plane). We may then align the reference basis so that $(\boldsymbol{\omega})_1 = 0 = (\boldsymbol{\omega})_3$ and $(\boldsymbol{\omega})_2 = \omega_{13}(\tau) = e_3^a g_{ab} \frac{De_1^b}{d\tau}$. Eq. (2.1) has the solution

$$s_1 + is_3 = S_\perp \exp\left(i \int^\tau \omega_{13}(\tau) d\tau\right), \quad s_2 = S_\parallel, \quad (2.3)$$

where S_\perp is a complex number satisfying $s^2 = |S_\perp|^2 + S_\parallel^2$, with S_\parallel real and constant. Thus, the precession angle Ψ accumulated over one radial period T is given by

$$\Psi = \int_0^T \omega_{13}(\tau) d\tau \quad (2.4)$$

where \mathcal{T} is the radial period with respect to proper time.

B. Discrete and continuous isometries

One may wish for a *geometric* definition of precession which does not depend on a choice reference basis. In curved space, a vector v^i parallel-transported around a closed path does not, in general, return to itself; and this immediately gives a geometric quantity. But in curved *spacetime*, timelike paths are not closed (except in pathological scenarios), so this procedure is not relevant.

For circular orbits, the spacetime and geodesic admit a continuous isometry (neglecting dissipative effects). That is, there exists a helical Killing vector field k^a for the spacetime which aligns with the tangent vector u^a on the geodesic. In Refs. [71, 72] a natural precession quantity was defined directly from the helical Killing field itself.

By contrast, for generic orbits, there is no continuous isometry. However, for eccentric orbits in the equatorial plane there is a *discrete* isometry, associated with the periodicity of the radial motion (neglecting dissipative effects). To make this notion more precise, let us adopt the passive viewpoint, in which there is a single spacetime (\mathcal{M}, g) with a local region covered by two coordinate systems x^a and x'^a , where the transformation between coordinates is sufficiently smooth that the usual transformation law applies, $g'_{ab} = \frac{\partial x'^c}{\partial x^a} \frac{\partial x'^d}{\partial x^b} g_{cd}$ (in the transformation law it is implicit that the left-hand and right-hand sides are evaluated at the same spacetime point). The spacetime possesses an isometry if the metric components in the two coordinate systems are equal when evaluated at *two different spacetime points which have the same coordinate values in the two systems*, $x'^c = x^c$. We may extend this concept to the worldline: under this coordinate transformation $z'^a(\tau') = \frac{\partial x^a}{\partial x'^b} z^b(\tau)$ where τ' is a function of τ , we demand that $z'^a(\tau' = \tau) = z^a(\tau)$.

To be more concrete, for equatorial eccentric orbits there is a discrete isometry under the linear transformation $t' = t - T$, $r' = r$, $\theta' = \theta$, $\phi' = \phi - \Phi$ and $\tau' = \tau - \mathcal{T}$, where T , \mathcal{T} and Φ are the coordinate time, proper time and orbital angle accumulated in passing from periapsis to periapsis.

How may we exploit the discrete isometry? We may restrict attention to reference bases that respect the isometry: tetrads $e_\alpha^a(\tau)$ transforming in the standard way $e_\alpha'^a(\tau') = \frac{\partial x^a}{\partial x'^b} e_\alpha^b(\tau)$, which satisfy $e_\alpha'^a(\tau' = \tau) = e_\alpha^a(\tau)$. Now consider a pair of such

tetrads within the isometry-respecting class, related by $\tilde{e}_1 + i\tilde{e}_3 = e^{i\varphi(\tau)}(e_1 + ie_3)$. It is straightforward to show, from Eq. (2.4), that $\tilde{\Psi} = \Psi - [\varphi(\mathcal{T}) - \varphi(0)]$. As both tetrads respect the isometry, the last term is, at worst, a multiple of 2π . We may eliminate this term by restricting attention to those triads that rotate once in passing around the black hole (like the spherical polar basis). Then, Ψ becomes insensitive to the choice of reference tetrad within a rather general class.

C. Geodetic spin precession for test bodies around black holes

1. Generic geodesics in Kerr spacetime

Consider the parallel transport of spin along a generic test-body geodesic with tangent vector u^a on the Kerr spacetime, in Boyer-Lindquist coordinates. The Kerr spacetime admits two Killing vectors, $X_{(t)}^a$ and $X_{(\phi)}^a$, satisfying $X_{(a;b)} = 0$, and one Killing-Yano tensor f_{ab} , satisfying $f_{(ab)} = 0$ and $f_{ab;c} = f_{[ab;c]}$. There are three constants of motion: energy $E = -X_{(t)}^a u_a$, azimuthal angular momentum $L = X_{(\phi)}^a u_a$, and the Carter constant $\mathcal{K} = \overleftrightarrow{f}_a^c f_{bc} u^a u^b + (L - aE)^2$ [95], in addition to the particle's mass m_1 .

The vector $q^a \equiv \overleftrightarrow{f}_b^a u^b$ is parallel-propagated along the geodesic ($u^b q_{a;b} = f_{ac;b} u^b u^c + f_{ac} u^b \overleftrightarrow{u}_{;b}^c = 0$) and orthogonal to the tangent vector ($u^a q_a = u^a f_{ab} u^b = 0$, by antisymmetry) [96]. Furthermore, its magnitude is set by the Carter constant: $q^a q_a = \mathcal{K}$.

Marck [97] introduced a standard tetrad e_α^a , with its zeroth leg along u^a and its second leg given by $e_2^a = q^a / \sqrt{\mathcal{K}}$. The standard tetrad is given explicitly in Eq. (29)–(30) of Ref. [97]. The geometric properties of the standard tetrad are explored in Ref. [98]. Relative to this basis, the precession frequency is

$$\omega_{13} = \frac{\mathcal{K}^{1/2}}{r^2 + a^2 \cos^2 \theta} \left(\frac{E(r^2 + a^2) - aL}{r^2 + K} + a \frac{L - aE \sin^2 \theta}{\mathcal{K} - a^2 \cos^2 \theta} \right). \quad (2.5)$$

2. Equatorial geodesics in Kerr spacetime

For orbits confined to the equatorial plane ($\theta = \pi/2$), the triad legs e_1^a , e_2^a and e_3^a are eigenvectors of the electric tidal tensor C_{ij} , with eigenvalues $-(2 + 3\mathcal{K}/r^2)m_2/r^3$, $(1 + 3\mathcal{K}/r^2)m_2/r^3$ and m_2/r^3 , respectively. Thus, the reference basis has local physical significance. The second triad leg e_2^a reduces to the unit vector orthogonal to the plane. In addition, e_α^a in the plane is a function of r and $\dot{r} = \frac{dr}{d\tau}$ only (and the constants of motion) and so it respects the discrete isometry (Sec. II B). The precession frequency reduces to

$$\omega_{13} = \frac{\sqrt{\mathcal{K}}}{r^2 + \mathcal{K}} \left(E + \frac{a}{L - aE} \right). \quad (2.6)$$

3. Equatorial geodesics in Schwarzschild spacetime

Hereforth, we shall assume the black hole is non-rotating ($a = 0$). In standard Schwarzschild coordinates $\{t, r, \theta, \phi\}$ the line element is $ds^2 = g_{ab} dx^a dx^b = -f dt^2 + f^{-1} dr^2 + r^2(d\theta^2 + r^2\phi^2)$, where $f(r) = 1 - 2M/r$. The Carter constant reduces to $\mathcal{K} = L^2$, and the precession frequency to $\omega_{13} = EL/(r^2 + L^2)$. Explicitly, the standard tetrad has the following components:

$$\begin{aligned} e_0^a &= u^a = [E/f, \dot{r}, 0, L/r^2], & e_2^a &= [0, 0, 1/r, 0], \\ e_1^a &= \frac{1}{f\sqrt{1 + L^2/r^2}} [\dot{r}, fE, 0, 0], & e_3^a &= \frac{1}{r\sqrt{1 + L^2/r^2}} [EL/f, L\dot{r}, 0, 1 + L^2/r^2], \end{aligned} \quad (2.7)$$

with $\dot{r} = u^r$ determined from the energy equation,

$$\dot{r}^2 = E^2 - f(1 + L^2/r^2). \quad (2.8)$$

A bound eccentric geodesic may be parametrized by

$$r(\chi) = \frac{p m_2}{1 + e \cos \chi}, \quad (2.9)$$

where χ is the relativistic anomaly, and p and e are the (dimensionless) semi-latus rectum and eccentricity. The dimensionless

energy E and angular momentum L are related to p and e by [86]

$$E = \left[\frac{(p-2-2e)(p-2+2e)}{p(p-3-e^2)} \right]^{1/2}, \quad L = \frac{pm_2}{\sqrt{p-3-e^2}}. \quad (2.10)$$

Expressions for $d\tau/d\chi$, $dt/d\chi$, and $d\phi/d\chi$ are given in Eq. (2.6), (2.7a) and (2.7b) of Ref. [86]. To these, we supplement

$$\frac{d\Psi}{d\chi} = \omega_{13} \frac{d\tau}{d\chi} = \sqrt{\frac{p-3-e^2}{p-6-2e\cos\chi}} \frac{\sqrt{(p-2-2e)(p-2+2e)}}{(p-2+2e\cos\chi-e^2\sin^2\chi)}. \quad (2.11)$$

We may find \mathcal{T} , T , Φ and Ψ by integrating over one radial period, e.g., $\Psi = \int_0^{2\pi} \frac{d\Psi}{d\chi} d\chi$. The orbital angle Φ is given in terms of an elliptic integral in Eq. (2.9) of Ref. [86],

$$\Phi = 4\sqrt{\frac{p}{p-6+2e}} \text{ellipK} \left(\frac{4e}{p-6+2e} \right). \quad (2.12)$$

The other quantities may not be written in a similarly compact form. However, one may easily calculate these numerically, or by expanding as a series in $1/p$ as follows:

$$\begin{aligned} \frac{\mathcal{T}}{2\pi v} = & \frac{1}{j_e^3} + \frac{3}{2j_e} p^{-1} + \left(\frac{3}{2} + \frac{6}{j_e} + \frac{3}{8} j_e \right) p^{-2} + \left(\frac{29}{2} + \frac{24}{j_e} + 3j_e + \frac{3}{4} j_e^2 - \frac{1}{16} j_e^3 \right) p^{-3} + \\ & + \left(\frac{96}{j_e} + \frac{1737}{16} + 18j_e + \frac{129}{16} j_e^2 - \frac{3}{4} j_e^3 - \frac{3}{16} j_e^4 + \frac{3}{128} j_e^5 \right) p^{-4} + \mathcal{O}(p^{-5}), \end{aligned} \quad (2.13)$$

$$\frac{T}{2\pi v} = \frac{1}{j_e^3} + \frac{3}{j_e} p^{-1} + \left(\frac{15}{2} + \frac{6}{j_e} \right) p^{-2} + \left(\frac{75}{2} + \frac{30-6e^2}{j_e} \right) p^{-3} + \left(\frac{3729}{16} + \frac{96}{j_e} + 30j_e - \frac{75}{16} j_e^2 \right) p^{-4} + \dots, \quad (2.14)$$

$$\frac{\Phi}{2\pi} = 1 + 3p^{-1} + \frac{27}{4} + \left(\frac{3}{4} e^2 \right) p^{-2} + \left(\frac{135}{2} + \frac{45}{4} e^2 \right) p^{-3} + \left(\frac{2835}{8} + \frac{945}{8} e^2 + \frac{105}{64} e^4 \right) p^{-4} + \mathcal{O}(p^{-5}), \quad (2.15)$$

$$\begin{aligned} \frac{\Psi}{2\pi} = & 1 + \frac{3}{2} p^{-1} + \left(\frac{63}{8} - \frac{3}{4} e^2 \right) p^{-2} + \left(\frac{675}{16} - \frac{21}{8} e^2 - \frac{3}{16} e^4 \right) p^{-3} + \\ & + \left(\frac{29403}{128} + \frac{363}{32} e^2 - \frac{249}{64} e^4 - \frac{3}{32} e^6 \right) p^{-4} + \mathcal{O}(p^{-5}), \end{aligned} \quad (2.16)$$

where $v = m_2 p^{\frac{3}{2}}$ and $j_e = \sqrt{1-e^2}$. Expansions for the redshift $z = \mathcal{T}/T$ and the spin precession $\psi = 1 - \Psi/\Phi$ follow immediately,

$$\begin{aligned} z = & 1 - \frac{3}{2} j_e^2 p^{-1} + j_e^3 \left(-6 + \frac{39}{8} j_e \right) p^{-2} + j_e^3 \left(-23 + 6j_e + 30j_e^2 - \frac{235}{16} j_e^3 \right) p^{-3} + \\ & + j_e^3 \left(-\frac{249}{2} + 24j_e + 174j_e^2 + 6j_e^3 - \frac{507}{4} j_e^4 + \frac{5643}{128} j_e^5 \right) p^{-4} + \mathcal{O}(p^{-5}), \end{aligned} \quad (2.17)$$

$$\begin{aligned} \psi = & \frac{3}{2} p^{-1} + \left(\frac{9}{8} + \frac{3}{2} e^2 \right) p^{-2} + \left(\frac{27}{16} + \frac{33}{4} e^2 + \frac{3}{16} e^4 \right) p^{-3} + \\ & + \left(\frac{405}{128} + \frac{705}{16} e^2 + \frac{123}{32} e^4 + \frac{3}{32} e^6 \right) p^{-4} + \mathcal{O}(p^{-5}). \end{aligned} \quad (2.18)$$

Note that, in the circular limit $e \rightarrow 0$, we have the exact results $z = \sqrt{1-3/p}$ and $\psi = 1 - \sqrt{1-3/p}$.

The radial and (average) azimuthal frequencies are defined via

$$\Omega_r = \frac{2\pi}{T}, \quad \Omega_\phi = \frac{\Phi}{T}. \quad (2.19)$$

The frequencies $\{\Omega_r, \Omega_\phi\}$ can be measured by an observer at infinity, and thus provide an unambiguous parametrization for eccentric orbits. By contrast, the semi-latus rectum p and eccentricity e are defined only in terms of the periapsis and apsis radii, which are not invariant under a change of radial coordinate.

III. Gravitational self-force method

In Sec. II we examined spin precession ψ in the test-body limit. We now consider a compact body with a finite mass $m_1 \ll m_2$ and a small spin $s_1 \ll (G/c)m_1^2$, orbiting a Schwarzschild black hole of mass m_2 , where m_1 and m_2 are the ADM masses.

A. Outline of scheme

We start by assuming that there exists a well-defined function $\psi(\Omega_r, \Omega_\phi, m_2, m_1)$, for *any* mass ratio $q = m_1/m_2$. We seek to isolate and compute the linear-in- m_1 part of this function using perturbation theory, that is,

$$\Delta\psi(\Omega_r, \Omega_\phi, m_2) \equiv [\psi(\Omega_r, \Omega_\phi, m_2, m_1) - \psi(\Omega_r, \Omega_\phi, m_2, 0)]_{\mathcal{O}(m_1)}, \quad (3.1)$$

where the square paranthesis denote the $\mathcal{O}(m_1)$ part. In this section, we shall denote test-body quantities using an overbar, i.e. $\bar{\Phi}, \bar{\Psi}, \bar{e}_\alpha^a$, etc.

Underpinning our approach is the key result that, through $\mathcal{O}(m_1)$, a small slow-spinning compact body follows a geodesic in a *regular perturbed spacetime* g_{ab}^R [25]; and, furthermore, its spin vector is parallel-transported in that same spacetime [32]. Here, we restrict to the small-spin regime $s \ll Gm_1^2/c$ and neglect Mathisson–Papapetrou terms [99, 100]. Note that g_{ab}^R is not the physical metric; rather, it is obtained by subtracting a certain ‘symmetric singular’ part from the physical metric, following the Detweiler–Whiting formulation [25] (details of the regularization procedure are given in Sec. III D 2). The regularly-perturbed metric can be written $g_{ab}^R = \bar{g}_{ab} + h_{ab}^R$, where \bar{g}_{ab} is the background Schwarzschild spacetime and $h_{ab}^R = \mathcal{O}(m_1)$ is the metric perturbation. Henceforth, we shall omit the superscript R .

In our perturbative approach, we shall compare quantities defined on a worldline γ in the regular perturbed spacetime (\mathcal{M}, g) with quantities on a reference worldline $\bar{\gamma}$ in a background spacetime $(\bar{\mathcal{M}}, \bar{g})$. In the regular-perturbed spacetime, we consider a geodesic (0) with proper time τ , worldline coordinates $z^\alpha(\tau)$, and orbital parameters p, e . In the background spacetime, there are at least three possible choices of reference worldline: (1) an accelerated worldline with (p, e) on the background spacetime with the coordinates $z^\alpha(\tau(\bar{\tau}))$, (2) a geodesic with (p_0, e_0) on the background which becomes (1) under the influence of gravitational self force, and (3) a geodesic with (p, e) on the background. In each case, the orbit may be parameterized using Eq. (2.9). Note that, for a given relativistic anomaly χ , the coordinate difference between (2) and (3) is $\mathcal{O}(m_1)$. Hence, at leading order in m_1 the instantaneous self-force computed on (3) is the same as on (2). Thus we may exclusively use (3) and dispense with (1) and (2).

We use the symbol δ to denote the difference at $\mathcal{O}(m_1)$ between a quantity on geodesic (0) and the same quantity on geodesic (3), implicitly making the choice $\bar{\chi} = \chi$ in the comparison, e.g. $\delta e_\alpha^a = e_\alpha^a(\chi) - \bar{e}_\alpha^a(\bar{\chi} = \chi)$. Since geodesics (0) and (3) have the same orbital parameters p, e , this implies that we are comparing at the same coordinate radius r , though not the same t and ϕ coordinates. We should emphasize that any such difference δY is *not* gauge-invariant, in general.

We will also use δ to denote the variation in those quantities which are defined via orbital integrals, such as \mathcal{T}, T, Φ and Ψ . Let Y denote some physical quantity defined by an integral around a geodesic, and let $y = dY/d\tau$ denote its local frequency. (For example, $Y \in \{\mathcal{T}, T, \Phi, \Psi\}$ and $y \in \{1, u^t, u^\phi, \omega_{13}\}$.) As in Sec. II C 3, the background quantity \bar{Y} is found by integrating \bar{y} from periapsis to periapsis,

$$\bar{Y} \equiv \int_0^{2\pi} \bar{y} \frac{d\bar{\tau}}{d\chi} d\chi. \quad (3.2)$$

The first-order variation δY is found via the integral

$$\delta Y = \int_0^{2\pi} \left(\frac{\delta y}{\bar{y}} - \frac{\delta u^r}{\bar{u}^r} \right) \bar{y} \frac{d\bar{\tau}}{d\chi} d\chi. \quad (3.3)$$

Barack & Sago [69] (henceforth BS2011) have shown how to apply the GSF formalism to calculate $\delta\Phi$ and δT for eccentric orbits, and thus also the frequency shifts $\delta\Omega_r = \delta(2\pi/T) = -(\delta T/T)\Omega_r$ and $\delta\Omega_\phi = \delta(\Phi/T) = (\delta\Phi/\bar{\Phi} - \delta T/\bar{T})\bar{\Omega}_\phi$. We will follow their approach, and extend it to calculate $\delta\Psi$.

Recall that we seek the $\mathcal{O}(q)$ shift *at fixed* Ω_r, Ω_ϕ (equivalently, fixed Φ and T), denoted by ΔY . This is given by

$$\Delta Y = \delta Y - \frac{\partial \bar{Y}}{\partial \bar{T}} \delta T - \frac{\partial \bar{Y}}{\partial \bar{\Phi}} \delta \Phi. \quad (3.4)$$

The latter terms may be found by applying the chain rule, i.e.,

$$\frac{\partial \bar{Y}}{\partial \bar{T}} = \frac{\partial \bar{Y}}{\partial p} \frac{\partial p}{\partial \bar{T}} + \frac{\partial \bar{Y}}{\partial e} \frac{\partial e}{\partial \bar{T}} \quad (3.5)$$

with $\{\frac{\partial p}{\partial \bar{T}}, \dots\}$ obtained by inverting $\{\frac{\partial \bar{T}}{\partial p}, \dots\}$.

It follows from the definition that $\Delta \bar{T} = \Delta \Phi = \Delta \Omega_r = \Delta \Omega_\phi = 0$. It follows from Eq. (1.1) that

$$\Delta \psi = -\frac{\Delta \Psi}{\Phi}. \quad (3.6)$$

(And it follows from $z \equiv \mathcal{T}/T$ that $\Delta z = \Delta \mathcal{T}/\bar{T}$). In sections below we focus on calculating $\delta \Psi$ and thus $\Delta \Psi$.

B. Circular orbit limit

Here we pause to consider the circular-orbit limit of $\Delta \psi$. Naively, one might expect $\lim_{e \rightarrow 0} \Delta \psi$ to reduce to $\Delta \psi^{\text{circ}}$, the quantity calculated for circular orbits in Refs. [71–75]. On the other hand, $\Delta \psi^{\text{circ}}$ is defined by comparing *circular* orbits in the perturbed and unperturbed spacetimes with the same azimuthal frequency Ω_ϕ , whereas $\Delta \psi$ is defined by comparing not-necessarily-circular orbits in the perturbed and unperturbed spacetimes with the same *pair* of frequencies Ω_ϕ and Ω_r . By fixing *both* frequencies, the orbit in the perturbed spacetime will not necessarily be circular even when the background orbit is so. As conceptually-different comparisons are made, it is plausible that $\lim_{e \rightarrow 0} \Delta \psi \neq \Delta \psi^{\text{circ}}$, and so it proves.

Let us consider the definitions in the $e \rightarrow 0$ limit,

$$\Delta \psi^{\text{circ}} = \delta \psi^{\text{circ}} - \frac{d\bar{\psi}^{\text{circ}}}{d\bar{\Omega}_\phi} \delta \Omega_\phi, \quad (3.7)$$

$$\lim_{e \rightarrow 0} \Delta \psi = \lim_{e \rightarrow 0} \delta \psi - \lim_{e \rightarrow 0} \left[\frac{\partial \bar{\psi}}{\partial \bar{\Omega}_r} \delta \Omega_r + \frac{\partial \bar{\psi}}{\partial \bar{\Omega}_\phi} \delta \Omega_\phi \right]. \quad (3.8)$$

It is straightforward to establish that the first terms are equal: $\delta \psi^{\text{circ}} = \lim_{e \rightarrow 0} \delta \psi$. On the other hand, the latter terms are not, and we are left with an offset term,

$$\lim_{e \rightarrow 0} \Delta \psi - \Delta \psi^{\text{circ}} = \frac{d\bar{\psi}^{\text{circ}}}{d\bar{\Omega}_\phi} \delta \Omega_\phi - \lim_{e \rightarrow 0} \left[\frac{\partial \bar{\psi}}{\partial \bar{\Omega}_r} \delta \Omega_r + \frac{\partial \bar{\psi}}{\partial \bar{\Omega}_\phi} \delta \Omega_\phi \right] \quad (3.9)$$

$$= -\frac{2(p-3)^{1/2}(p-6)^{5/2}}{p(4p^2-39p+86)} \frac{\Delta \Phi^{\text{circ}}}{2\pi}, \quad (3.10)$$

where $\Delta \Phi^{\text{circ}} = \delta \Phi - \frac{d\bar{\Phi}}{d\bar{\Omega}_\phi} \delta \Omega_\phi$. We recognise $\Delta \Phi^{\text{circ}}/(2\pi)$ as the $\mathcal{O}(q)$ part of the periapsis advance per unit angle K [69]. It is a physical quantity which is gauge-invariant (in the usual GSF sense), and it has been calculated elsewhere. The significance of this quantity in GSF theory, pN theory and numerical relativity was explored in Ref. [70].

C. Formulation

For notational simplicity, we now drop the over-bar notation for denoting background quantities.

1. Perturbation of the tetrad

We start by writing the perturbed tetrad e_α^a in the following way,

$$\begin{aligned} \delta u^a &= \delta e_0^a = c_{00} u^a + c_{01} e_1^a + c_{03} e_3^a, \\ \delta e_1^a &= c_{10} u^a + c_{11} e_1^a + c_{13} e_3^a, \\ \delta e_3^a &= c_{30} u^a + c_{31} e_1^a + c_{33} e_3^a. \end{aligned} \quad (3.11)$$

where $c_{\alpha\beta}$ are coefficients at $\mathcal{O}(m_1)$, to be deduced. (N.B. the second leg e_2^a remains orthogonal to the orbital plane.) Now we impose the orthogonality conditions $g_{ab} e_\alpha^a e_\beta^b = \eta_{\alpha\beta}$, to deduce that

$$\begin{aligned} c_{00} &= \frac{1}{2} h_{00} & c_{11} &= -\frac{1}{2} h_{11}, & c_{33} &= -\frac{1}{2} h_{33}, \\ c_{10} &= h_{01} + c_{01}, & c_{30} &= h_{03} + c_{03}, & c_{13} + c_{31} &= -h_{13}, \end{aligned} \quad (3.12)$$

where

$$h_{\alpha\beta} \equiv h_{ab}e_{\alpha}^a e_{\beta}^b. \quad (3.13)$$

The tangent vector ($u^a = e_0^a$) may be written in the following form,

$$u^a = [f^{-1}(E + \delta E), \dot{r} + \delta \dot{r}, 0, (L + \delta L)/r^2]. \quad (3.14)$$

The quantities δE etc. are straightforwardly related to the quantities $\hat{\delta}E$ etc. used in BS2011 [69] (appearing there as ΔE , etc.), via $\delta E = \frac{1}{2}h_{00}E + \hat{\delta}E$, etc. (The difference arises because BS2011 use a tangent vector \hat{u}^a normalized on the background spacetime, whereas we prefer a tangent vector normalized on the perturbed spacetime.) Note that the quantities $\hat{\delta}E$, $\hat{\delta}L$ and $\hat{\delta}\dot{r}$ are functions of χ , i.e., they are *not* constants. A procedure for calculating $\hat{\delta}E$ and $\hat{\delta}L$ is given in Ref. [69], and $\hat{\delta}\dot{r}$ may be deduced from the normalization condition

$$E\hat{\delta}E - \dot{r}\hat{\delta}\dot{r} - \frac{f(r)}{r^2}L\hat{\delta}L = 0. \quad (3.15)$$

Comparing Eq. (3.14) with Eq. (3.11) yields

$$c_{01} = \frac{E\dot{r}}{f\sqrt{1+L^2/r^2}} \left(\frac{\hat{\delta}\dot{r}}{\dot{r}} - \frac{\hat{\delta}E}{E} \right), \quad c_{03} = \frac{\hat{\delta}L}{r\sqrt{1+L^2/r^2}}. \quad (3.16)$$

Inserting Eq. (3.16) into Eq. (3.11) determines the tetrad, up to the single degree of freedom implicit in $c_{13} + c_{31} = -h_{13}$. This local ambiguity is to be expected, as we are free to locally rotate the reference basis in the 13 plane. The ambiguity is removed by considering the secular change over radial period, using the discrete isometry.

2. Perturbation of precession frequency

Now we turn attention to the leading-order variation of the precession frequency. As $\omega_{13} = g_{ab}e_3^a \frac{De_1^b}{d\tau}$ is antisymmetric in its indices, we shall consider the variation of $\omega_{(13)}$ and $\omega \equiv \omega_{[13]}$ separately. The former is identically zero, and it merely provides a validation check of our implementation. Applying the variation operator δ , and using the product rule $\delta(AB) = A\delta B + B\delta A$, yields

$$0 = \frac{1}{4}\omega(h_{33} - h_{11}) + g_{ab}e_{(3}^a \delta \left(\frac{De_{1)}^b}{d\tau} \right), \quad (3.17)$$

$$\delta\omega = \frac{1}{4}\omega(h_{33} + h_{11}) + g_{ab}e_{[3}^a \delta \left(\frac{De_{1]}^b}{d\tau} \right). \quad (3.18)$$

Here we have used the background identities $\frac{Du^a}{d\tau} = 0$, $\frac{De_1^a}{d\tau} = \omega e_3^a$ and $\frac{De_3^a}{d\tau} = -\omega e_1^a$, and Eq. (3.12). The last terms need more careful consideration. We obtain

$$0 = \frac{1}{2}\omega(h_{33} - h_{11}) - \frac{1}{2}\frac{dh_{13}}{d\tau} + \delta\Gamma_{(31)0}, \quad (3.19)$$

$$\delta\omega = \frac{1}{2}\omega h_{00} + \delta\Gamma_{[31]0} + (c_{01}e_1^b + c_{03}e_3^b)e_{a[3}\nabla_b e_{1]}^a + \frac{1}{2}\frac{d(c_{13} - c_{31})}{d\tau}, \quad (3.20)$$

where

$$\delta\Gamma_{[31]0} \equiv \overleftrightarrow{\delta\Gamma}_{cd}^a e_{a[3} e_{1]}^c u^d = \left(\delta\Gamma_{abc} - h_{ad}\overleftrightarrow{\Gamma}_{bc}^d \right) e_{[3}^a e_{1]}^b u^c, \quad (3.21)$$

with $\delta\Gamma_{abc} \equiv \frac{1}{2}(h_{ab,c} + h_{ac,b} - h_{bc,a})$.

Let us make several brief observations on Eqs. (3.19)–(3.20): (i) Eq. (3.19) is simply an identity, as can be verified by noting that $\delta\Gamma_{(31)0} = \frac{1}{2}e_3^a e_1^b u^c \nabla_c h_{ab} = \frac{1}{2}u^c \nabla_c h_{13} + \frac{1}{2}\omega h_{11} - \frac{1}{2}\omega h_{33}$; (ii) Eq. (3.20) is not uniquely defined in a local sense, due to the ambiguity in the last term (the freedom to locally rotate the tetrad), but this ambiguity is eliminated once we integrate over a radial period and impose the discrete isometry condition; (iii) for the case of circular orbits, Eq. (3.20) agrees with Eq. (2.65) of Ref. [73] (noting the difference in notation used in Ref. [73], $(\delta\Gamma)_{\bar{3}\bar{0}\bar{1}} = \delta\Gamma_{310} + h_{ad}\overleftrightarrow{\Gamma}_{bc}^d e_3^a e_1^b u^c$, and neglecting the final term); and (iv) the penultimate term in Eq. (3.20) requires the background tetrad to be treated as a field, rather than just a basis on the

background worldline itself.

Let us consider point (iv) in more detail. For given E, L , the background tetrad field is a function of r only, with $\dot{r}(r)$ interpreted as a function of r determined from the energy condition, $\dot{r}^2(r) = E^2 - f(r)(1 + L^2/r^2)$. The tetrad is defined everywhere within $p/(1 + e)$ and $p/(1 - e)$; it is orthonormal everywhere; and e_0^a is tangent to a geodesic everywhere in this region. Explicitly,

$$c_{01}e_1^b e_{a[3} \nabla_b e_{1]}^a = \frac{\omega}{fr(1 + L^2/r^2)} \left[\left(1 + \frac{L^2}{r^2} \right)^2 - \frac{E^2 L^2}{r} \right] \left(\frac{\hat{\delta}r}{\dot{r}} - \frac{\hat{\delta}E}{E} \right), \quad (3.22)$$

$$c_{03}e_3^b e_{a[3} \nabla_b e_{1]}^a = \omega \left(\frac{1 + 2L^2/r^2}{1 + L^2/r^2} \right) \frac{\hat{\delta}L}{L}. \quad (3.23)$$

To proceed, we may insert Eq. (3.20) with Eqs. (3.22)–(3.23) into the integral formula,

$$\delta\Psi = \int_0^{2\pi} \left(\frac{\delta\omega}{\omega} - \frac{\delta\dot{r}}{\dot{r}} \right) \omega \frac{d\tau}{d\chi} d\chi. \quad (3.24)$$

We then find $\Delta\Psi$ using Eq. (3.4), i.e. $\Delta\Psi = \delta\Psi - \frac{\partial\bar{\Psi}}{\partial T}\delta T - \frac{\partial\bar{\Psi}}{\partial\Phi}\delta\Phi$, and insert this into Eq. (3.6) to obtain $\Delta\psi$.

D. Numerical computation

Below we describe the numerical implementation of the GSF method (III D 1) and the regularization procedure (III D 2).

1. Implementation details

We perform the numerical computation using the GSF code of Ref. [101] which employs a frequency-domain approach, with the method of extended homogeneous solutions [102], to compute the components of the regularized metric perturbation h_{ab}^R in Lorenz gauge. This code has already been used (i) to evolve EMRIs via the osculating geodesics method in Ref. [103], (ii) to obtain a large set of eccentric-orbit data for the redshift invariant in Ref. [86], and (iii) to numerically determine the EOB \bar{d} and q potentials in Ref. [66]. We have developed the code to compute, in addition, the scalars $h_{11}, h_{33}, \delta\Gamma_{130}, \delta\Gamma_{310}$ in Eqs. (3.20, 3.19). We have also calculated the regularization parameters for these quantities which we present in Sec. III D 2.

The code samples the interval $\chi \in [0, 2\pi]$ at 240 evenly spaced points χ_i where it outputs $h_{00}, h_{11}, h_{33}, F_t^{\text{cons}}, F_\phi^{\text{cons}}, \delta\Gamma_{130}$ and $\delta\Gamma_{310}$ at double floating point precision. Here, $F_{t,\phi}^{\text{cons}}$ are the conservative parts of the t, ϕ components of the GSF. We use *Mathematica*'s `Interpolation` function to convert the discrete data sets into continuous functions suitable for numerical integration. We use two different orders of interpolation, three and six, and calculate $\Delta\psi$. The change in $\Delta\psi$ arising from this difference is our estimated interpolation error for $\Delta\psi$.

The interpolated data is sufficiently smooth for numerical integration. However, there are a few troublesome terms that come from double numerical integrals that arise from the c_{01}, c_{03} terms. These are functions of $\hat{\delta}E(\chi), \hat{\delta}L(\chi), \hat{\delta}\dot{r}(\chi)$ each of which is an integral of the components of the GSF as given by BS2011

$$\hat{\delta}E(\chi) = \hat{\delta}E(0) - \underbrace{\int_0^\chi d\chi' F_t^{\text{cons}}(\chi') \frac{d\tau}{d\chi'}}_{\equiv \mathcal{E}(\chi)}, \quad \hat{\delta}L(\chi) = \hat{\delta}L(0) + \underbrace{\int_0^\chi d\chi' F_\phi^{\text{cons}}(\chi') \frac{d\tau}{d\chi'}}_{\equiv \mathcal{L}(\chi)}, \quad (3.25)$$

where $\hat{\delta}E(0), \hat{\delta}L(0)$ are the $\mathcal{O}(m_1)$ corrections to energy and angular momentum at the periapsis as explained by BS2011. $\hat{\delta}\dot{r}(\chi)$ can be obtained from Eq. (3.15). Each of these terms are in turn integrated over a radial period in Eq. (3.24), which can be problematic. We deal with this issue by first algebraically simplifying the coefficients of $\mathcal{E}(\chi), \mathcal{L}(\chi)$ then by replacing the numerical values of the $\chi = 0, \pi$ endpoints of the integrand in Eq. (3.24) with analytical limits. More specifically, we first rewrite $\delta\omega$ using Eqs. (3.22, 3.23). Then, we use $\delta\omega^r = \frac{1}{2}h_{00}\dot{r} + \hat{\delta}\dot{r}$ in Eq. (3.24) to remove the $\frac{1}{2}\omega h_{00}$ term in Eq. (3.20). Finally, we rewrite the remaining terms proportional to $\hat{\delta}\dot{r}$ in terms of $\hat{\delta}E$ and $\hat{\delta}L$ using Eq. (3.15). In the end, we are left with a term of the form

$$f_1(\chi) \frac{\mathcal{E}(\chi) + \mathcal{L}(\chi)}{\sin^2 \chi} + f_2(\chi) \frac{\mathcal{E}(\pi) + \mathcal{L}(\pi)}{4 \cos^2 \frac{\chi}{2}} + f_3(\chi), \quad (3.26)$$

where f_1, f_2, f_3 depend only on background quantities and are regular at $\chi = 0, \pi$. Although Eq. (3.26) looks like it diverges at $\chi = 0, \pi$, the analysis in BS2011 has proven these endpoints to be removable singularities. Therefore, we can replace the

divergent values by the analytic limits at $\chi = 0, \pi$. The details of this procedure are provided in BS2011. Let us just mention that this replacement requires evaluating $dF_t^{\text{cons}}/d\chi, dF_\phi^{\text{cons}}/d\chi$ at $\chi = 0, \pi$ which we can obtain in a straightforward manner using one-sided finite-difference derivative formulae.

The GSF code uses several approximations and truncations which we explain next. The method of extended homogeneous solutions constructs the spherical-harmonically decomposed fields $h_{ab}^{R,lm}(t, r)$ (time-domain solutions) by summing over the Fourier modes of radial motion labeled by n . By construction, the n sum converges exponentially, however, we can only compute a finite number of n modes. So we truncate the n sum by imposing a convergence criterion based on the C^0 continuity of the $h_{ab}^{R,lm}(t, r)$ at $r = r(\chi) \equiv r_p$: with each n mode added to the sum we consider the difference $dh \equiv |[h_{ab}^{R,lm}(t, r \rightarrow r_p^-) - h_{ab}^{R,lm}(t, r \rightarrow r_p^+)]/h_{ab}^{R,lm}(t, r_p)|$ and terminate the n mode computation once dh reaches some prechosen threshold value. Similarly, we also truncate the infinite sum over the multipole modes at some $l = l_{\max}$ since the regularized modes $h_{ab}^{R,l}$ ¹ scale as l^{-2} so this sum converges, albeit slowly [104]. We approximate the remaining contribution to the l sum by constructing fits to the last five to ten numerically computed l modes and choosing the best fit that minimizes the appropriate χ -square. This procedure is standard for mode-sum GSF calculations and the resulting fit is referred to as the l -mode tail. The details of how to calculate it can be found in, e.g., Ref. [101].

At each $\{p, e\}$ we run our code to produce four data sets with $\{dh, l_{\max}\} = \{10^{-9}, 15\}, \{10^{-10}, 20\}, \{5 \times 10^{-10}, 18\}, \{5 \times 10^{-10}, 20\}$, which yield four different values for $\Delta\psi$. Recall that the raw data is discrete in χ thus is interpolated using two different orders so in the end we end up with eight different values for each $\Delta\psi(p, e)$. Our final result for $\Delta\psi(p, e)$ is the mean value of this set and the error we quote is the difference between the maximum and minimum values. Other errors are subdominant.

Finally, we must deal with the fact that Lorenz gauge is not asymptotically flat, i.e. $\lim_{r \rightarrow \infty} h_{tt}^{\text{Reg}, l=0} = -2\alpha \neq 0$, where α is a constant. This gauge ‘unpleasantness’ can be removed by transforming the original Lorenz-gauge time coordinate by $t \rightarrow t(1 + \alpha)$. This shift in t manifests itself in the orbital period T hence in the orbital frequencies Ω_r, Ω_ϕ . Returning to Eq. (3.4) and inserting this correction yields

$$\Delta\psi = \delta\psi - (1 + \alpha) \frac{\partial\bar{\psi}}{\partial\bar{T}} \delta T - (1 - \alpha) \frac{\partial\bar{\psi}}{\partial\bar{\Phi}} \delta\Phi. \quad (3.27)$$

This ‘flat-fixing’ or ‘flattening-out’ has become standard in Lorenz-gauge GSF computations and must be done regardless of the type of motion. Indeed, this correction was first done for circular orbits [52]. The details of this correction for eccentric orbits can be found in Sec. III.B of BS2011. α can be computed to arbitrary precision from the monopole solution which is obtained analytically in the frequency domain [101]. Without this correction, one can not obtain the correct result for any invariant that one computes in Lorenz gauge.

We present our numerical results for $\Delta\psi$ in Table II for eccentric orbits with $p = \{10, 15, 20, 25, \dots, 115, 120\}$ and $e = \{0.05, 0.075, 0.1, \dots, 0.225, 0.25\}$. We include our code’s circular-orbit result, $\Delta\psi_\odot$, at the top row of each sub-table. Recall that $\Delta\psi_\odot \neq \Delta\psi(e \rightarrow 0)$ hence the sign disagreement between the $e = 0$ and $e > 0$ values. For each value $\Delta\psi(p, e)$ we display the leading digit of the corresponding error in parentheses. For example, our result for $\Delta\psi(p = 10, e = 0)$ should be read as $5.9385659 \times 10^{-3} \pm 5 \times 10^{-10}$. We present analysis and plots in Sec. V

2. Regularization

We employ the standard method of mode-sum regularization. Schematically, an unregularized quantity X^{full} with ℓ -modes $X_{\ell\pm}^{\text{full}}$ in the limit $r \rightarrow r_0^\pm$ is converted to a regularized quantity X^R using

$$X^R = \sum_{\ell=0}^{\infty} [X_{\ell\pm}^{\text{full}} - (2\ell + 1)A^\pm - B]. \quad (3.28)$$

The regularization parameters A^\pm and B for the relevant quantities in Eq. (3.20) are listed in Table I. We note that all A^\pm coefficients vanish.

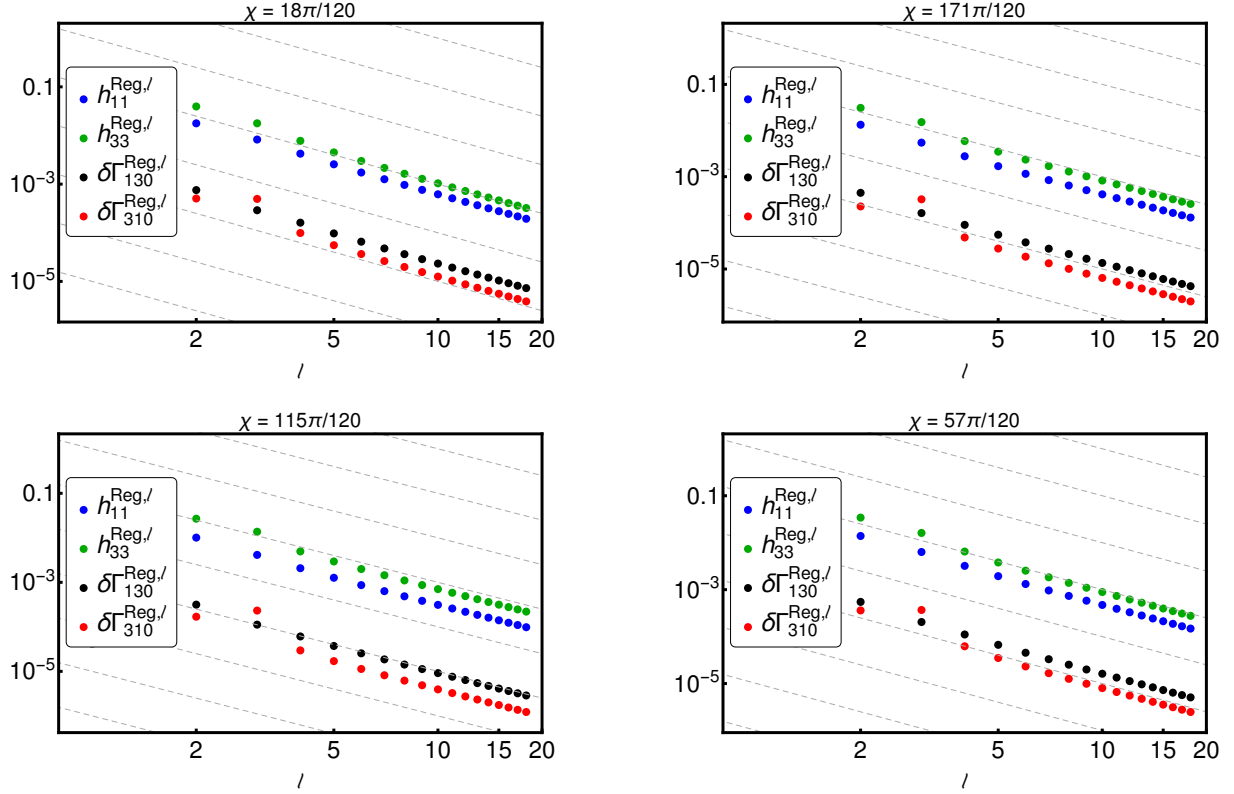
To obtain the regularization parameters (RPs) for each quantity in Table I, we started with RPs for the spacetime components of metric perturbation and its partial derivatives with respect to Schwarzschild coordinates. These were calculated by B. Wardell

¹ $h_{ab}^{R,l}$ are obtained from $\sum_m Y^{lm}(\pi/2, \phi) h_{ab}^{R,lm}$.

	A^\pm	B
h_{00}, h_{11}, h_{33}	0	$\frac{4}{\pi\sqrt{r^2+L^2}}\text{ellipK}\left(\frac{L^2}{r^2+L^2}\right)$
h_{01}, h_{03}, h_{13}	0	0
$\delta\Gamma_{[31]0}$	0	$\frac{4E}{\pi L\sqrt{r^2+L^2}}\left[\text{ellipE}\left(\frac{L^2}{r^2+L^2}\right) - \text{ellipK}\left(\frac{L^2}{r^2+L^2}\right)\right]$

TABLE I. Regularization parameters for metric components and first derivatives.

[105] using the approach developed in Refs. [106–109]. We label these RPs by $A_{ab} = 0, B_{ab}, A_{abc}, B_{abc}$ consistent with Eq. (3.28), where the rank-3 RPs are for $\partial_c h_{ab}$. Using the background tetrad we construct the appropriate RPs for h_{11}, h_{33} etc. which we label by B_{11}, B_{33} etc. We find that $A_{130} = A_{310} = 0$, which is noteworthy since the $\delta\Gamma$ terms constituted sums of up to 15 different terms for $\partial_c h_{ab}$. This was further confirmed by our numerical data for the unregularized l modes for $\delta\Gamma_{130,310}$ which approached constant values as $l \rightarrow \infty$. If $A \neq 0$ then we would have observed linear-in- l growth for these unregularized modes. In Fig. 1 we show the regularized l modes of $\{h_{11}, h_{33}, \delta\Gamma_{130}, \delta\Gamma_{310}\}$ at four randomly chosen χ values along an eccentric orbit with $p = 15, e = 0.15$ and $l_{\max} = 18$. As expected, the regularized l modes display an l^{-2} powerlaw for all cases that we present.

FIG. 1. Log-log plots showing the regularized l modes of $\{h_{11}, h_{33}, \delta\Gamma_{130}, \delta\Gamma_{310}\}$ at four randomly chosen χ values along an eccentric orbit with $p = 15$ and $e = 0.15$ and $l_{\max} = 18$. The diagonal grid lines are l^{-2} curves consistent with Eq. (3.28).

IV. Post-Newtonian expansion

In this section we arrive at the key result that, at next-to-next-to-leading-order (NNLO), the post-Newtonian expansion of the spin precession scalar through $\mathcal{O}(q)$, $\psi = \bar{\psi} + \Delta\psi + \mathcal{O}(q^2)$, is given by

$$\bar{\psi} = \frac{3}{2}p^{-1} + \left(\frac{9}{8} + \frac{3}{2}e^2\right)p^{-2} + \left(\frac{27}{16} + \frac{33}{4}e^2 + \frac{3}{16}e^4\right)p^{-3} + \mathcal{O}(p^{-4}), \quad (4.1)$$

$$q^{-1}\Delta\psi = -p^{-1} + \left(\frac{9}{4} + e^2\right)p^{-2} + \left[\frac{739}{16} - \frac{123\pi^2}{64} + \left(\frac{341}{16} - \frac{123\pi^2}{256}\right)e^2 - \frac{e^4}{2}\right]p^{-3} + \mathcal{O}(p^{-4}). \quad (4.2)$$

In Sec. V we verify that the post-Newtonian result appears to be consistent with the GSF calculation of Sec. III.

The spin-orbit (SO) Hamiltonian in ADM coordinates was presented in Ref. [92] at NLO and extended to NNLO in Refs. [93, 94]. The Hamiltonian takes the simple form $H_{SO} = \sum_{i=1}^2 \Omega_i \cdot \mathbf{S}_i$ where Ω_i are spin-precession frequencies with respect to coordinate time. For equatorial orbits, $\Omega_1 = \frac{\partial H_{SO}}{\partial \mathbf{S}_1} = \Omega_S \mathbf{k}$ where \mathbf{k} is a unit vector orthogonal to the equatorial plane, and $\Omega_S = \Omega_{S2} + \Omega_{S4} + \Omega_{S6} + \mathcal{O}(c^{-8})$. Here Ω_{S2} , Ω_{S4} and Ω_{S6} are the contributions at LO (c^{-2}), NLO (c^{-4}), and NNLO (c^{-6}), respectively.

The spin precession invariant is defined as

$$\psi = \frac{\langle \Omega_S \rangle}{\langle \Omega_\phi \rangle}, \quad (4.3)$$

where $\langle \cdot \rangle$ denotes the orbital average over one radial period. (The difference between Eq. (4.3) and Eq. (1.1) is simply due to defining precession with respect to a Cartesian-type basis as opposed to a polar-type basis). For circular orbits, ψ has previously been calculated through NNLO in Ref. [110], Eq. (4.5) and Ref. [71], Eq. (9).

Our calculation is based on the approach in Sec. IV of Ref. [86]. We perform the calculation in the centre-of-mass frame. The orbital average is taken using the generalized quasi-Keplerian (QK) representation introduced in [111], which is known up to 3pN in both harmonic and ADM coordinates [112], and which is described in Sec. IVC of [86].

To illustrate the procedure, let us consider only the leading-order term, $\Omega_{S2} = \frac{G}{c^2 r^2} \left(\frac{3m_2}{2m_1} \mathbf{n}_{12} \times \mathbf{p}_1 - 2\mathbf{n}_{12} \times \mathbf{p}_2 \right)$. In the centre of mass frame we have $\mathbf{p}_1 = -\mathbf{p}_2 = \mathbf{p}$ and $\mathbf{n}_{12} \times \mathbf{p}_1 = \frac{L}{r} \mathbf{k}$, where L is the angular momentum. Thus, $\Omega_{S2} = \frac{gL}{c^2 r^3}$ where $g = (3 + 3\Delta + 2\nu)/4\nu$ is the gyro(gravito)magnetic ratio, with $\nu \equiv m_1 m_2 / m^2$ the symmetric mass ratio, $\Delta \equiv (m_2 - m_1)/m$ the reduced mass difference, and $m \equiv m_1 + m_2$ the total mass.

Our task is to compute the orbital averages using the QK representation. The mean anomaly $\ell = \Omega(t - t_{\text{per}})$ and the eccentric anomaly u give the parametrization $r(u) = a_r(1 - e_r \cos u)$ and $\ell(u) = u - e_t \sin u + f_t \sin V + g_t(V - u)$, through NNLO. Here, Ω_r , a_r , e_t , e_r , f_t and g_t are QK orbital elements, and $V(u)$ is specified in Eq. (4.20) of [86]. The QK representation is only complete once the orbital elements are specified in terms of orbital integrals. Following [113] we use the dimensionless coordinate-invariant quantities

$$\varepsilon \equiv -\frac{2\tilde{E}}{c^2}, \quad j \equiv -\frac{2\tilde{E}\tilde{L}^2}{(Gm)^2}, \quad (4.4)$$

where $\tilde{E} = E/\mu$ and $\tilde{L} = L/\mu$ are the binding energy and orbital angular momentum, respectively, per reduced mass $\mu \equiv m_1 m_2 / m = \nu m$. Noting that $\varepsilon = \mathcal{O}(c^{-2})$ and $j = \mathcal{O}(c^0)$ allows one to keep track of pN orders. The various QK elements are expanded in powers of ε in Eqs. (4.22) of Ref. [86].

By way of illustration, let us consider $\langle \Omega_{S2} \rangle = gGLc^{-2} \langle r^{-3} \rangle$. At NLO, we may neglect f_t and g_t which scale as $e_t \sim f_t \sim \mathcal{O}(\varepsilon^2)$; thus

$$\langle r^{-3} \rangle = \frac{\Omega_r}{2\pi} \int_0^{2\pi} \frac{1}{r(u)^3} \frac{dt}{d\ell} \frac{d\ell}{du} du, \quad (4.5)$$

$$\Rightarrow \langle r^{-3} \rangle^{NLO} = \frac{1}{2\pi a_r^3} \int_0^{2\pi} \frac{1 - e_t \cos u}{(1 - e_r \cos u)^3} du = \frac{2 + e_r^2 - 3e_r e_t}{2a_r^3 (1 - e_r^2)^{5/2}}. \quad (4.6)$$

To extend to NNLO, we must include the f_t and g_t terms; the resulting integrals are straightforward with the help of Mathematica. Other orbital averages such as $\langle r^{-4} \rangle$, $\langle r^{-5} \rangle$ and $\langle p_r^2 r^{-3} \rangle$ etc. may be found in a similar way.

We are led to an expression for the spin precession scalar which is valid for *any* mass ratio. We may write $\psi = \psi^{LO} + \psi^{NLO} + \psi^{NNLO}$, with

$$\psi^{LO} = \frac{\varepsilon}{j} \left(\frac{3}{4} + \frac{3}{4}\Delta + \frac{\nu}{2} \right), \quad (4.7)$$

$$\begin{aligned} \psi^{NLO} &= \frac{\varepsilon^2}{j^2} \left\{ \left(\frac{3}{4} + \frac{3}{4}\Delta + \frac{\nu}{2} \right) \left[\frac{(48 - 15\nu - 18j + 13\nu j)}{4} \right] + \frac{(j-3) [5\Delta^2 + 2\Delta(3\nu + 5) - 8\nu^2 + 6\nu + 5]}{4(\Delta + 1)} \right. \\ &\quad \left. + \frac{(j-1)(\Delta - 2\nu + 1) [5\Delta^2 + \Delta(10 - 44\nu) - 36\nu^2 - 44\nu + 5]}{32(\Delta + 1)^2} \right\} \end{aligned}$$

$$+ \frac{(\Delta+1)^2(3j-5)[5\Delta^2 + \Delta(10-32\nu) - 12\nu^2 - 32\nu + 5]}{128(\Delta-2\nu+1)} \Bigg\}. \quad (4.8)$$

The term $\psi^{NNLO} = \mathcal{O}(\varepsilon^3)$ term is lengthy and will be presented elsewhere. To obtain the NNLO result, one needs an appropriate expression for the radial momentum p_r . Starting with Eq. (5.6) of Ref. [114] and taking derivatives with respect to the components of the relative velocity [115], one gets

$$p_r^2 = \mu^2 \dot{r}^2 \left[1 + c^{-2} \left\{ (1-3\nu)(\dot{r}^2 + r^2 \dot{\phi}^2) + \frac{Gm}{r} (6+4\nu) \right\} + \mathcal{O}(c^{-4}) \right], \quad (4.9)$$

where the overdot denotes differentiation with respect to coordinate time.

The next step is to decompose ψ into $\mathcal{O}(q^0)$ and $\mathcal{O}(q^1)$ parts, for comparison with the GSF result. First, we note that ε and j are defined in Eq. (4.4) in terms of energy and angular momentum, rather than the frequencies Ω_r and Ω_ϕ used in the GSF approach. Following [113], we introduce the dimensionless coordinate-invariant parameters,

$$x = \left(\frac{Gm\Omega_\phi}{c^3} \right)^{2/3}, \quad \iota \equiv \frac{3x}{k}, \quad (4.10)$$

where $k = K - 1$ with $K = \Omega_\phi/\Omega_r$. We replace (ε, j) with (x, ι) using Eqs. (4.40) in Ref. [86]. Next, following [86], we introduce a pair of parameters (y, λ) better suited to the extreme mass-ratio limit $q \ll 1$, defined as $y \equiv (Gm_2\Omega_\phi/c^3)^{2/3}$ and $\lambda = 3y/k$, so that $x = (1+q)^{2/3}y$ and $\iota = (1+q)^{2/3}\lambda$. After this replacement we expand ψ as a series in q , to isolate the $\mathcal{O}(q^0)$ and $\mathcal{O}(q^1)$ parts. That is, we write $\bar{\psi}$ and $\Delta\psi$ as functions of (y, λ) . Finally, we switch to orbital elements (p, e) which are defined with respect to the frequencies Ω_ϕ and Ω_r using the functional relationships on the background spacetime. As these relationships cannot be inverted analytically, we make use of the series expansions (B1) in [86].

At the end of this process we reach Eqs. (4.1) and (4.2): relative 2pN expansions for $\bar{\psi}$ and $\Delta\psi$. It is also straightforward to find higher-order-in- q contributions, $\Delta\psi_{q^2}$ etc., if required for validation of any (future) second-order GSF calculation.

The pN series pass three consistency checks. First, the pN series for $\bar{\psi}$, Eq. (4.1), is in accord with the series expansion of ψ on the background spacetime, Eq. (2.18). Second, in the circular limit $e \rightarrow 0$, the difference between $\Delta\psi$ in Eq. (4.2) and $\Delta\psi^{\text{circ}}$ given by the μ/M part of Eq. (10) in Ref. [71] is found to be precisely the pN series for the offset term in Eq. (3.10). Finally, the pN series (4.2) appears to be consistent with the GSF numerical results for $\Delta\psi$, as we now show.

V. Results

Here we present a selection of numerical results from the GSF method (Sec. III) and compare with the post-Newtonian series (Sec. IV).

A. Numerical data for $\Delta\psi$

Sample GSF data for $\Delta\psi$ is given in Table II, for orbital parameters $10 \leq p \leq 120$ and $0 \leq e \leq 0.25$.

TABLE II: Numerical data for $\Delta\psi$. First column labels the eccentricity while the remaining columns label different p values. In the rows corresponding to $e = 0.000$ we present the circular-orbit output of our code, $\Delta\psi_{\odot}$, which can be compared with Table III of Ref. [73] or with 17.5-pN expressions of Ref. [75]. Note that $\Delta\psi_{\odot} \neq \Delta\psi(e \rightarrow 0)$ (see Sec. III B). Here we use the standard GSF error notation where the last digit in the parentheses for each value indicates the error at the decimal point of the last digit. For example, $5.9385659(5) \times 10^{-3} = 5.9385659 \times 10^{-3} \pm 5 \times 10^{-10}$.

e	$p = 10$	$p = 15$	$p = 20$	$p = 25$	$p = 30$	$p = 35$
0.000	$5.9385659(5) \times 10^{-3}$	$3.3750158(2) \times 10^{-3}$	$2.07150085(7) \times 10^{-3}$	$1.38686308(2) \times 10^{-3}$	$9.9003322(2) \times 10^{-4}$	$7.4105684(1) \times 10^{-4}$
0.050	$-5.061140(3) \times 10^{-2}$	$-4.914075(5) \times 10^{-2}$	$-4.123078(1) \times 10^{-2}$	$-3.4789491(6) \times 10^{-2}$	$-2.989822(2) \times 10^{-2}$	$-2.6143411(7) \times 10^{-2}$
0.075	$-5.052269(7) \times 10^{-2}$	$-4.911220(2) \times 10^{-2}$	$-4.1217013(8) \times 10^{-2}$	$-3.4781485(9) \times 10^{-2}$	$-2.989305(3) \times 10^{-2}$	$-2.613978(1) \times 10^{-2}$
0.100	$-5.039852(2) \times 10^{-2}$	$-4.907223(7) \times 10^{-2}$	$-4.119775(5) \times 10^{-2}$	$-3.477028(1) \times 10^{-2}$	$-2.988568(7) \times 10^{-2}$	$-2.613468(2) \times 10^{-2}$
0.125	$-5.023891(2) \times 10^{-2}$	$-4.902089(2) \times 10^{-2}$	$-4.1172994(7) \times 10^{-2}$	$-3.475587(2) \times 10^{-2}$	$-2.987639(1) \times 10^{-2}$	$-2.6128112(8) \times 10^{-2}$
0.150	$-5.004439(5) \times 10^{-2}$	$-4.895813(2) \times 10^{-2}$	$-4.114274(3) \times 10^{-2}$	$-3.473827(2) \times 10^{-2}$	$-2.986492(2) \times 10^{-2}$	$-2.6120105(4) \times 10^{-2}$
0.175	$-4.98131(5) \times 10^{-2}$	$-4.888402(2) \times 10^{-2}$	$-4.1107001(2) \times 10^{-2}$	$-3.471747(2) \times 10^{-2}$	$-2.9851407(5) \times 10^{-2}$	$-2.611063(2) \times 10^{-2}$
0.200	$-4.95475(2) \times 10^{-2}$	$-4.879857(9) \times 10^{-2}$	$-4.106580(2) \times 10^{-2}$	$-3.469348(1) \times 10^{-2}$	$-2.983580(3) \times 10^{-2}$	$-2.609973(3) \times 10^{-2}$
0.225	$-4.92468(5) \times 10^{-2}$	$-4.870169(8) \times 10^{-2}$	$-4.101909(1) \times 10^{-2}$	$-3.466629(1) \times 10^{-2}$	$-2.981813(3) \times 10^{-2}$	$-2.608738(2) \times 10^{-2}$
0.250	$-4.89105(9) \times 10^{-2}$	$-4.859358(1) \times 10^{-2}$	$-4.096689(7) \times 10^{-2}$	$-3.463592(2) \times 10^{-2}$	$-2.979840(1) \times 10^{-2}$	$-2.607352(2) \times 10^{-2}$
e	$p = 40$	$p = 45$	$p = 50$	$p = 55$	$p = 60$	$p = 65$
0.000	$5.7505234(1) \times 10^{-4}$	$4.5900246(1) \times 10^{-4}$	$3.7475920(1) \times 10^{-4}$	$3.11703594(6) \times 10^{-4}$	$2.6329573(1) \times 10^{-4}$	$2.2533310(3) \times 10^{-4}$
0.050	$-2.319599(1) \times 10^{-2}$	$-2.083062(1) \times 10^{-2}$	$-1.889476(3) \times 10^{-2}$	$-1.728324(2) \times 10^{-2}$	$-1.5922111(9) \times 10^{-2}$	$-1.475776(2) \times 10^{-2}$

TABLE II: (continued)

0.075	$-2.3193296(3) \times 10^{-2}$	$-2.082857(2) \times 10^{-2}$	$-1.8893114(1) \times 10^{-2}$	$-1.728196(2) \times 10^{-2}$	$-1.5920996(3) \times 10^{-2}$	$-1.475687(2) \times 10^{-2}$
0.100	$-2.318953(2) \times 10^{-2}$	$-2.0825685(1) \times 10^{-2}$	$-1.889085(5) \times 10^{-2}$	$-1.728011(1) \times 10^{-2}$	$-1.591948(2) \times 10^{-2}$	$-1.475553(2) \times 10^{-2}$
0.125	$-2.3184703(2) \times 10^{-2}$	$-2.082198(1) \times 10^{-2}$	$-1.888792(1) \times 10^{-2}$	$-1.727773(2) \times 10^{-2}$	$-1.591752(1) \times 10^{-2}$	$-1.4753912(8) \times 10^{-2}$
0.150	$-2.3178794(6) \times 10^{-2}$	$-2.081744(3) \times 10^{-2}$	$-1.888434(2) \times 10^{-2}$	$-1.727486(2) \times 10^{-2}$	$-1.591513(2) \times 10^{-2}$	$-1.4751887(9) \times 10^{-2}$
0.175	$-2.3171815(9) \times 10^{-2}$	$-2.0812102(5) \times 10^{-2}$	$-1.8880110(6) \times 10^{-2}$	$-1.727142(2) \times 10^{-2}$	$-1.5912302(2) \times 10^{-2}$	$-1.4749509(6) \times 10^{-2}$
0.200	$-2.316378(2) \times 10^{-2}$	$-2.080592(2) \times 10^{-2}$	$-1.887523(2) \times 10^{-2}$	$-1.726748(1) \times 10^{-2}$	$-1.590903(3) \times 10^{-2}$	$-1.474681(1) \times 10^{-2}$
0.225	$-2.315467(3) \times 10^{-2}$	$-2.079894(5) \times 10^{-2}$	$-1.886970(2) \times 10^{-2}$	$-1.7263003(9) \times 10^{-2}$	$-1.590534(3) \times 10^{-2}$	$-1.4743701(5) \times 10^{-2}$
0.250	$-2.314445(3) \times 10^{-2}$	$-2.079112(2) \times 10^{-2}$	$-1.886353(2) \times 10^{-2}$	$-1.725800(1) \times 10^{-2}$	$-1.590122(2) \times 10^{-2}$	$-1.474022(2) \times 10^{-2}$
<i>e</i>	<i>p</i> = 70	<i>p</i> = 75	<i>p</i> = 80	<i>p</i> = 85	<i>p</i> = 90	<i>p</i> = 95
0.000	$1.950169674(6) \times 10^{-4}$	$1.7042571(5) \times 10^{-4}$	$1.5020480(2) \times 10^{-4}$	$1.33377732(1) \times 10^{-4}$	$1.1922590(3) \times 10^{-4}$	$1.0721120(2) \times 10^{-4}$
0.050	$-1.375078(2) \times 10^{-2}$	$-1.2871695(4) \times 10^{-2}$	$-1.209737(7) \times 10^{-2}$	$-1.141067(2) \times 10^{-2}$	$-1.079745(9) \times 10^{-2}$	$-1.024652(1) \times 10^{-2}$
0.075	$-1.375006(2) \times 10^{-2}$	$-1.287096(2) \times 10^{-2}$	$-1.2096987(8) \times 10^{-2}$	$-1.141016(2) \times 10^{-2}$	$-1.0796893(5) \times 10^{-2}$	$-1.024593(2) \times 10^{-2}$
0.100	$-1.374891(4) \times 10^{-2}$	$-1.2869985(9) \times 10^{-2}$	$-1.2096001(4) \times 10^{-2}$	$-1.140936(2) \times 10^{-2}$	$-1.079628(9) \times 10^{-2}$	$-1.024536(2) \times 10^{-2}$
0.125	$-1.3747508(6) \times 10^{-2}$	$-1.2868785(9) \times 10^{-2}$	$-1.209502(1) \times 10^{-2}$	$-1.140867(2) \times 10^{-2}$	$-1.079537(2) \times 10^{-2}$	$-1.024473(2) \times 10^{-2}$
0.150	$-1.374583(3) \times 10^{-2}$	$-1.286731(1) \times 10^{-2}$	$-1.209375(3) \times 10^{-2}$	$-1.1407409(8) \times 10^{-2}$	$-1.079445(6) \times 10^{-2}$	$-1.0243993(6) \times 10^{-2}$
0.175	$-1.3743806(6) \times 10^{-2}$	$-1.2865597(2) \times 10^{-2}$	$-1.209224(3) \times 10^{-2}$	$-1.140611(1) \times 10^{-2}$	$-1.0793214(9) \times 10^{-2}$	$-1.024262(2) \times 10^{-2}$
0.200	$-1.374145(5) \times 10^{-2}$	$-1.286350(4) \times 10^{-2}$	$-1.209044(5) \times 10^{-2}$	$-1.140452(2) \times 10^{-2}$	$-1.079193(2) \times 10^{-2}$	$-1.024162(3) \times 10^{-2}$
0.225	$-1.373887(3) \times 10^{-2}$	$-1.286132(2) \times 10^{-2}$	$-1.208854(7) \times 10^{-2}$	$-1.140282(4) \times 10^{-2}$	$-1.079042(4) \times 10^{-2}$	$-1.024012(2) \times 10^{-2}$
0.250	$-1.373589(2) \times 10^{-2}$	$-1.285874(2) \times 10^{-2}$	$-1.208622(2) \times 10^{-2}$	$-1.140082(4) \times 10^{-2}$	$-1.078859(2) \times 10^{-2}$	$-1.023867(2) \times 10^{-2}$
<i>e</i>	<i>p</i> = 100	<i>p</i> = 105	<i>p</i> = 110	<i>p</i> = 115	<i>p</i> = 120	
0.000	$9.692429(3) \times 10^{-5}$	$8.8049204(2) \times 10^{-5}$	$8.0339083(2) \times 10^{-5}$	$7.359865(2) \times 10^{-5}$	$6.7671891(9) \times 10^{-5}$	
0.050	$-9.7486(2) \times 10^{-3}$	$-9.2978299(9) \times 10^{-3}$	$-8.885264(2) \times 10^{-3}$	$-8.509223(2) \times 10^{-3}$	$-8.161612(2) \times 10^{-3}$	
0.075	$-9.747944(3) \times 10^{-3}$	$-9.296404(3) \times 10^{-3}$	$-8.885037(2) \times 10^{-3}$	$-8.508608(2) \times 10^{-3}$	$-8.1619099(3) \times 10^{-3}$	
0.100	$-9.747837(2) \times 10^{-3}$	$-9.296183(2) \times 10^{-3}$	$-8.884334(3) \times 10^{-3}$	$-8.507611(1) \times 10^{-3}$	$-8.161921(1) \times 10^{-3}$	
0.125	$-9.7470611(8) \times 10^{-3}$	$-9.295938(2) \times 10^{-3}$	$-8.883748(1) \times 10^{-3}$	$-8.506629(1) \times 10^{-3}$	$-8.161265(3) \times 10^{-3}$	
0.150	$-9.746265(4) \times 10^{-3}$	$-9.294971(3) \times 10^{-3}$	$-8.883078(7) \times 10^{-3}$	$-8.506364(2) \times 10^{-3}$	$-8.159340(2) \times 10^{-3}$	
0.175	$-9.745473(4) \times 10^{-3}$	$-9.293686(7) \times 10^{-3}$	$-8.8823995(5) \times 10^{-3}$	$-8.50557(1) \times 10^{-3}$	$-8.160131(5) \times 10^{-3}$	
0.200	$-9.74441(6) \times 10^{-3}$	$-9.293319(7) \times 10^{-3}$	$-8.88132(1) \times 10^{-3}$	$-8.50498(1) \times 10^{-3}$	$-8.158818(1) \times 10^{-3}$	
0.225	$-9.74322(4) \times 10^{-3}$	$-9.29210(3) \times 10^{-3}$	$-8.88076(3) \times 10^{-3}$	$-8.503858(6) \times 10^{-3}$	$-8.15786(2) \times 10^{-3}$	
0.250	$-9.74155(3) \times 10^{-3}$	$-9.29094(4) \times 10^{-3}$	$-8.87957(2) \times 10^{-3}$	$-8.50296(7) \times 10^{-3}$	$-8.15717(2) \times 10^{-3}$	

B. Analysis and comparisons with pN results

In this section we set $q = 1$ for simplicity. We begin by checking the consistency of our result for $\Delta\psi(e \rightarrow 0)$ given by Eq. (3.8) with our numerical data and the pN derivation. To this end we consider the quantity given by $\Delta\psi - \Delta\psi_{e^2} - \Delta\psi_{e^4}$, where

$$\Delta\psi_{e^2} = \left[1 + \left(\frac{341}{16} - \frac{123\pi^2}{256} \right) \frac{1}{p} \right] \frac{1}{p^2} \approx \frac{1}{p^2} + \frac{16.5705}{p^3}, \quad (5.1)$$

$$\Delta\psi_{e^4} = -\frac{e^4}{2p^3}, \quad (5.2)$$

which are the e -dependent parts of Eq. (4.2). Clearly, $\Delta\psi - \Delta\psi_{e^2} - \Delta\psi_{e^4} = \lim_{e \rightarrow 0} \Delta\psi + a_4/p^4 + a_4^{\log} \log p/p^4 + \mathcal{O}(p^{-5})$ where the unknown terms will be obtained analytically from a future 3pN computation for ψ^{NNNLO} . Nonetheless, our code has just enough accuracy to extract the following values for their coefficients: $a_4 = -108 \pm 2$, $a_4^{\log} = 50.0 \pm 0.6$, respectively. Our error bars are probably slightly optimistic, however we are confident of the signs and the magnitudes of these two terms. We leave the more accurate numerical extraction of these parameters for future work.

In Fig. 2 we display a log-log plot of $\Delta\psi - \Delta\psi_{e^2} - \Delta\psi_{e^4}$ represented by the blue dots. This is compared with post-Newtonian approximations $\Delta\psi^{LO}(e \rightarrow 0)$, $\Delta\psi^{NLO}(e \rightarrow 0)$, $\Delta\psi^{NNLO}(e \rightarrow 0)$ (dotted black, dot-dashed green and dashed blue lines). The red curve represents $\lim_{e \rightarrow 0} \Delta\psi$. The $\mathcal{O}(p^{-4}, p^{-4} \log p)$ offset between the red curve and the blue dots is too small to be discerned in the main plot so we show it in the inset as the blue dots after multiplying by p^4 . The brown band crossing all the

blue dots of the inset is our two-parameter fit: $a_4 + a_4^{\log} \log p$ with best-fit values quoted above. Our numerical errors are much smaller than the size of the blue dots in the figure so they can not be seen in the main plot, but they manifest themselves as the width of the brown band plotted in the inset.

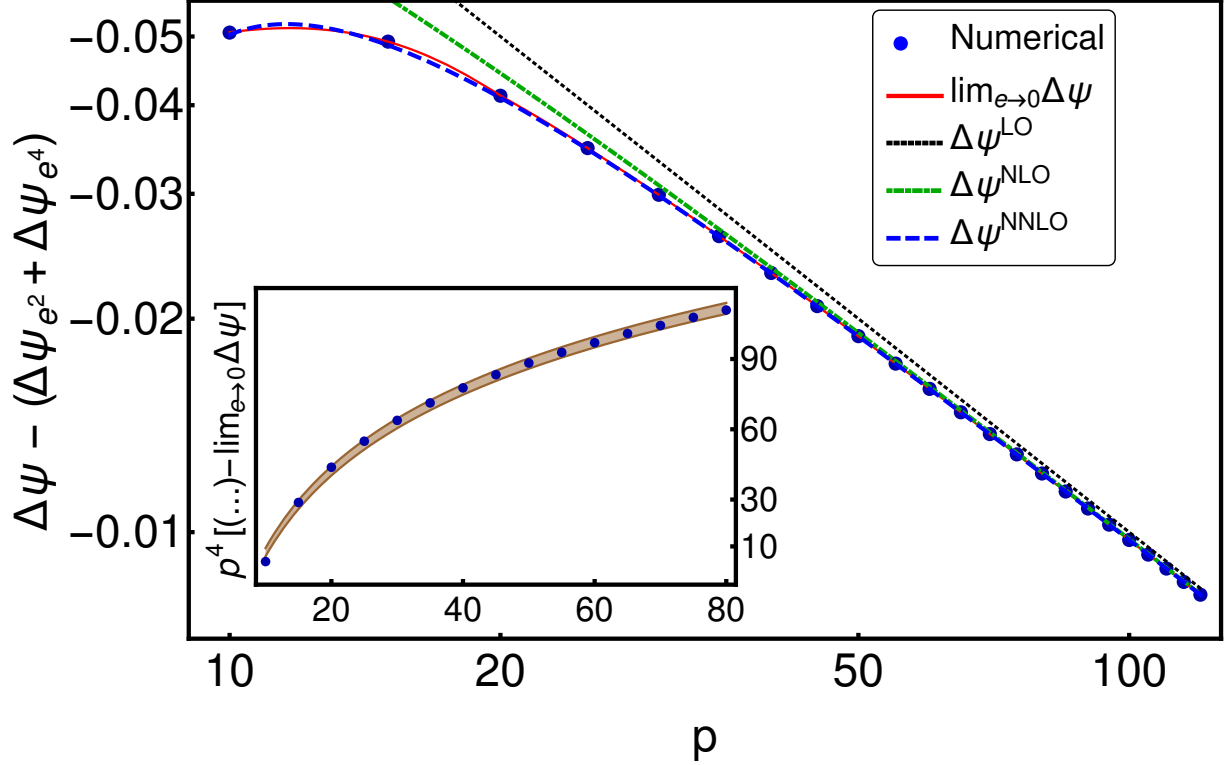


FIG. 2. Comparison of $\Delta\psi - \Delta\psi_{e^2} - \Delta\psi_{e^4}$ (blue dots) with $\lim_{e \rightarrow 0} \Delta\psi$ (solid red curve) where the difference is $\mathcal{O}(p^{-4}, p^{-4} \log p)$ hence too small to distinguish in the main plot so we show it in the inset as the blue dots after multiplying by p^4 . $\Delta\psi_{e^2}$ is given by Eq. (5.1), $\Delta\psi_{e^4} = -e^4/(2p^3)$ and $\lim_{e \rightarrow 0} \Delta\psi$ is given by Eq. (3.8). The post-Newtonian approximations $\Delta\psi^{LO}(e \rightarrow 0)$, $\Delta\psi^{NLO}(e \rightarrow 0)$, $\Delta\psi^{NNLO}(e \rightarrow 0)$ are plotted as the dotted black, dot-dashed green and dashed blue lines, respectively. Our numerical errors are much smaller than the size of the blue dots in the figure so we do not display them in the main plot, but they manifest themselves as the width of the brown band plotted in the inset, which is our fit $a_4 + a_4^{\log} \log p$ with best-fit parameters $a_4 = -108 \pm 2$, $a_4^{\log} = 50.0 \pm 0.6$. The (...) in the vertical-axis label of the inset equals $\Delta\psi - \Delta\psi_{e^2} - \Delta\psi_{e^4}$.

Next, we show results for our numerically extracted values for $\Delta\psi_{e^2}$ which we compare with Eq. (5.1) in Fig. 3 where we present eight plots for $p^2 \Delta\psi_{e^2} \approx 1 + 16.5705/p$ with $e = \{0.075, 0.1, 0.125, \dots, 0.25\}$. The black dots represent our numerical values, the red dashed line represents the 1pN result ($=1$) and the solid blue curve the 2pN result ($\approx 1 + 16.5705/p$). For visualization purposes, we connect the black dots with a thin green shaded region representing our estimated error, but this error ‘band’ is only meaningful at p values for which we present data in Table II (though we suspect that the width of the green curve is representative of the errors in regions for which we presently do not have data.) As the plot shows, our numerical results contain some information about the unknown 3pN $\mathcal{O}(e^2/p^4)$ term for which we provide numerical estimations in the next paragraph. This term is the cause of the offset between the green curve (connecting the black dots) and the blue curve in Fig. 3. Moreover, the fact that the curves cross further hints at a sign change in the pN series. As expected, this offset decreases as p increases. Note that our data for $p^2 \Delta\psi_{e^2}$ becomes noisy for $p \gtrsim 100$ and smaller values of e as indicated by the upper half of the plots in Fig. 3. In this regime, the magnitude of $16.5705 e^2/p^3$ becomes comparable to our error.

With our analytical 1 pN knowledge i.e. the e^2/p^2 term, we now use our data to make a numerical estimation for the values of the known 2-pN (≈ 16.5705) and unknown 3 and 4-pN parameters. To do so, we compute $p^3 e^{-2} [\Delta\psi - \lim_{e \rightarrow 0} \Delta\psi]$ for all $\{p, e\}$ and construct fits to this quantity of the form $c_2 + c_3/p + c_4/p^2 + \dots$ using the ‘clean’ portion of our data i.e. $p \leq 45$. We vary the number of fit parameters from two to five and obtain the best fits using standard χ^2 -minimizing techniques. Our best-fit results give

$$c_2 = 15.84 \pm 0.59 \text{ vs. } 16.5705 \dots,$$

$$c_3 = -52.05 \pm 17.8, \text{ and } c_4 = 780 \pm 40. \quad (5.3)$$

Our value for c_2 is consistent with our analytical 2pN result and as we predicted, the 3pN term has the opposite sign to the 2pN term. The unknown 4pN term is positive and our various fits yield a range of values for it from $\sim 10^2$ to 10^3 so the error bar we quote for this quantity in Eq. (5.3) is probably too optimistic. We present our findings in Fig. 4 where the green (noisy) shaded region is our numerically extracted ‘zone’ for $p^3 e^{-2} [\Delta\psi - \lim_{e \rightarrow 0} \Delta\psi]$. The thick, red line marks the analytically known 2pN parameter equaling $16.5705\dots$. The black region between the two dashed black curves is our estimation up to 3pN from Eq. (5.3), and similarly the blue region between the two solid, blue lines is our estimated 4pN result. Here, we do not attempt to estimate the coefficients of the log terms that start showing up at ≥ 3 pN, which we leave to future work. Inserting all the numerically estimated parameters into Eq. (4.2) results in the following expression

$$\begin{aligned} q^{-1} \Delta\psi = -p^{-1} + \left(\frac{9}{4} + e^2 \right) p^{-2} + \left[\frac{739}{16} - \frac{123\pi^2}{64} + \left(\frac{341}{16} - \frac{123\pi^2}{256} \right) e^2 - \frac{e^4}{2} \right] p^{-3} \\ + [-108(2) + 50.0(6) \log p - 52(18) e^2] p^{-4} + \mathcal{O}(p^{-5}). \end{aligned} \quad (5.4)$$

To make a really good estimation of the pN parameters we need to perform the numerical extractions at large p and small e , ideally $p > 1000$ and $e < 10^{-3}$, but our Lorenz-gauge code is not intended for weak-field, near-circular applications where our errors become comparable to the magnitude of the pN terms.

Let us conclude by adding that we can not currently numerically estimate the coefficient of the $\mathcal{O}(e^4/p^3)$ term at all. At our current range of eccentricities of $e \leq 0.25$ the magnitude of this term is always less than our estimated error for $\Delta\psi$. A reasonable numerical estimation of this term requires several improvements which we explain in detail in Sec. VI.

VI. Discussion

In the preceding sections we have computed the spin precession scalar ψ for eccentric compact binaries via two complementary approaches. In the GSF approach, we obtained ψ in the strong-field regime at $\mathcal{O}(q)$, whereas in the pN approach we obtained ψ at arbitrary mass ratio q as an expansion in powers of c^{-2} in the weak-field. We have established definitively that the results are in agreement at (separately) $\mathcal{O}(q^0)$; at $\mathcal{O}(q^1)$ in the circular limit; and at $\mathcal{O}(qe^2 p^{-2})$. We also obtained good agreement at $\mathcal{O}(qe^2 p^{-3})$ and the correct sign at $\mathcal{O}(qe^2 p^{-4})$ with a reasonable estimation for the magnitude of the relevant coefficient as given by the error bars Eq. (5.3). Our code is also able to pick up the non-log and log terms at $\mathcal{O}(qe^0 p^{-4})$ with an error of $\lesssim 2\%$.

Figure 4 illustrates our current limitations for the computation of $\Delta\psi$ with our Lorenz-gauge code. Be that as it may, the blue and black regions, which represent our numerical estimations for the $\mathcal{O}(qe^2 p^{-4})$, $\mathcal{O}(qe^2 p^{-5})$ terms, are consistent with our numerical data and our expectation of a negative term at $\mathcal{O}(qe^2 p^{-4})$.

We propose that $\Delta\psi$ should now be calculated via further complementary approaches. One possibility is to apply the *radiation-gauge* GSF architecture to compute ψ for eccentric orbits at much greater numerical precision [43, 44]. Another possibility is to use S. Hopper’s doubly-expanded (in p, e) expressions for h_{ab} and its derivatives to obtain a pN expression for $\Delta\psi$ accurate to $\mathcal{O}(e^{10})$ and $\mathcal{O}(p^{-5})$ [87, 116]. A third possibility is to extend the approach of Bini, Damour & collaborators [76, 77, 79, 81] making expert use of the Mano-Suzuki-Takasugi formalism [117].

Extending the *arbitrary mass ratio* pN calculation of ψ to next order (NNNLO) presents a stiff challenge. The NNNLO spin-orbit Hamiltonian has not appeared in the literature, but in principle, H_{SO} at NNNLO can be obtained from the 3pN equations of motion for non-spinning binaries [115].

The boundary between GSF and numerical relativity is under active exploration. Recently, the redshift invariant z was extracted from numerical relativity simulations of quasi-circular black hole binaries, via the helical (quasi-)Killing vector field [59]. It is plausible that the circular-orbit precession invariant ψ^{circ} can be extracted from the derivatives of the helical Killing vector field (see Eq. (3) in Ref. [71]). Obtaining the eccentric-orbit precession invariant poses a harder challenge as, in the absence of a continuous symmetry, it is necessary to track the spin of the small black hole in some sufficiently coordinate-insensitive way.

Our prescription for computing the spin precession invariant $\Delta\psi$ is, at present, far less elegant than that available for computing the redshift invariant Δz . Remarkably, in Ref. [86] it was shown that $\Delta z = -\langle H \rangle z$, where $\langle H \rangle = \frac{1}{T} \int_0^T \frac{1}{2} h_{00} d\tau$. This offered a significant simplification of the earlier prescription of Ref. [69], leading to improved numerical accuracy and physical insight. It is natural to wonder whether a similar simplification may be possible for the spin-precession calculation. To consider this, let us recap the argument for z . First, following the approach of Sec. III A, and using Eqs. (2.8), (3.3) and (3.15), one may quickly establish that $\delta\mathcal{T} = E\delta T - L\delta\Phi - \int_0^T \frac{1}{2} h_{00} d\tau$. Second, it follows from the definition of Δ that

$\Delta z = \Delta(\mathcal{T}/T) = \Delta\mathcal{T}/T$ (with $\Delta T = 0$ by definition). Third, combining Eq. (3.4) with the first step yields

$$\Delta\mathcal{T} = \delta\mathcal{T} - \frac{\partial\mathcal{T}}{\partial T}\delta T - \frac{\partial\mathcal{T}}{\partial\Phi}\delta\Phi, \quad (6.1)$$

$$= - \int_0^T \frac{1}{2} h_{00} d\tau + \left(E - \frac{\partial\mathcal{T}}{\partial T} \right) \delta T + \left(-L - \frac{\partial\mathcal{T}}{\partial\Phi} \right) \delta\Phi. \quad (6.2)$$

Finally, it may be shown using the first law of binary mechanics [60] that the two bracketed terms are identically zero (see Appendix B of [86]), and thus the simple result for Δz follows. Thus, it seems that we lack two crucial ingredients to transfer the recipe for Δz to $\Delta\psi$. First, an appropriate analogue of the energy equation (2.8) involving Ψ , and second, an appropriate analogue of the first law. It is possible that the laws of binary mechanics for spinning bodies [61] can provide the missing insight here.

In summary, we have taken one more small step in extracting physical content from GSF theory, to move further towards the goal of accurately modelling the gravitational two-body problem. There remain many challenges ahead: from transcribing eccentric-orbit GSF results into EOB theory, to calculating invariants for eccentric orbits on Kerr, and, most importantly, extending GSF theory to second order in the mass ratio. Progress is being made on a range of fronts, inspired by the successes of LIGO and eLISA Pathfinder which herald a new era of gravitational wave astronomy.

Acknowledgments

S.A. acknowledges support from the Irish Research Council, funded under the National Development Plan for Ireland. S.D. acknowledges support under EPSRC Grant No. EP/M025802/1, and from the Lancaster-Manchester-Sheffield Consortium for Fundamental Physics under STFC Grant No. ST/L000520/1. We are indebted to Alexandre Le Tiec for his assistance with the PN calculation (Sec. IV), and for discussions and correspondence relating to Sec. II A and Sec. III B. We are indebted to Barry Wardell for calculating previously-unpublished regularization parameters for h_{ab} on eccentric orbits (Sec. III D 2). S.A. also thanks Chris Kavanagh, Seth Hopper and Niels Warburton.

[1] B. P. Abbott *et al.* (Virgo, LIGO Scientific), *Phys. Rev. Lett.* **116**, 061102 (2016), arXiv:1602.03837 [gr-qc].
[2] B. P. Abbott *et al.* (Virgo, LIGO Scientific), *Phys. Rev. Lett.* **116**, 241103 (2016), arXiv:1606.04855 [gr-qc].
[3] B. P. Abbott *et al.* (Virgo, LIGO Scientific), (2016), arXiv:1606.04856 [gr-qc].
[4] K. Belczynski, D. E. Holz, T. Bulik, and R. O’Shaughnessy, *Nature* **534**, 512 (2016), arXiv:1602.04531 [astro-ph.HE].
[5] M. Armano *et al.*, *Phys. Rev. Lett.* **116**, 231101 (2016).
[6] P. Amaro-Seoane *et al.*, *Gravitational waves. Numerical relativity - data analysis. Proceedings, 9th Edoardo Amaldi Conference, Amaldi 9, and meeting, NRDA 2011, Cardiff, UK, July 10-15, 2011*, *Class. Quant. Grav.* **29**, 124016 (2012), arXiv:1202.0839 [gr-qc].
[7] L. Barack and C. Cutler, *Phys. Rev. D* **69**, 082005 (2004), arXiv:gr-qc/0310125 [gr-qc].
[8] P. Amaro-Seoane, J. R. Gair, A. Pound, S. A. Hughes, and C. F. Sopuerta, *Proceedings, 10th International LISA Symposium, J. Phys. Conf. Ser.* **610**, 012002 (2015), arXiv:1410.0958 [astro-ph.CO].
[9] U. Sperhake, *Class. Quant. Grav.* **32**, 124011 (2015), arXiv:1411.3997 [gr-qc].
[10] C. O. Lousto and Y. Zlochower, *Phys. Rev. Lett.* **106**, 041101 (2011), arXiv:1009.0292 [gr-qc].
[11] C. M. Will, *Proc. Nat. Acad. Sci.* **108**, 5938 (2011), arXiv:1102.5192.
[12] L. Bernard, L. Blanchet, A. Bohé, G. Faye, and S. Marsat, *Phys. Rev. D* **93**, 084037 (2016), arXiv:1512.02876 [gr-qc].
[13] T. Damour, P. Jaranowski, and G. Schäfer, *Phys. Rev. D* **93**, 084014 (2016), arXiv:1601.01283 [gr-qc].
[14] E. Poisson, A. Pound, and I. Vega, *Living Rev. Rel.* **14**, 7 (2011), arXiv:1102.0529.
[15] L. Barack, *Class. Quant. Grav.* **26**, 213001 (2009), arXiv:0908.1664.
[16] J. Thornburg, *GW Notes* **5**, 3 (2011), arXiv:1102.2857 [gr-qc].
[17] A. Pound, *Proceedings, 524th WE-Heraeus-Seminar: Equations of Motion in Relativistic Gravity (EOM 2013)*, *Fund. Theor. Phys.* **179**, 399 (2015), arXiv:1506.06245 [gr-qc].
[18] Y. Mino, M. Sasaki, and T. Tanaka, *Phys. Rev. D* **55**, 3457 (1997), arXiv:gr-qc/9606018.
[19] T. C. Quinn and R. M. Wald, *Phys. Rev. D* **56**, 3381 (1997), arXiv:gr-qc/9610053.
[20] T. Regge and J. A. Wheeler, *Physical Review* **108**, 1063 (1957).
[21] F. J. Zerilli, *Phys. Rev. D* **2**, 2141 (1970).
[22] S. A. Teukolsky, *Phys. Rev. Lett.* **29**, 1114 (1972).
[23] P. L. Chrzanowski, *Phys. Rev. D* **11**, 2042 (1975).

[24] L. Barack, Y. Mino, H. Nakano, A. Ori, and M. Sasaki, *Phys. Rev. Lett.* **88**, 091101 (2002), arXiv:gr-qc/0111001 [gr-qc].

[25] S. L. Detweiler and B. F. Whiting, *Phys. Rev. D* **67**, 024025 (2003), arXiv:gr-qc/0202086.

[26] I. Vega and S. L. Detweiler, *Phys. Rev. D* **77**, 084008 (2008), arXiv:0712.4405 [gr-qc].

[27] S. R. Dolan and L. Barack, *Phys. Rev. D* **83**, 024019 (2011), arXiv:1010.5255 [gr-qc].

[28] B. Wardell and N. Warburton, *Phys. Rev. D* **92**, 084019 (2015), arXiv:1505.07841 [gr-qc].

[29] A. Pound and E. Poisson, *Phys. Rev. D* **77**, 044013 (2008), arXiv:0708.3033 [gr-qc].

[30] T. Hinderer and E. E. Flanagan, *Phys. Rev. D* **78**, 064028 (2008), arXiv:0805.3337 [gr-qc].

[31] A. Pound, *Phys. Rev. D* **81**, 024023 (2010), arXiv:0907.5197 [gr-qc].

[32] A. I. Harte, *Class. Quant. Grav.* **29**, 055012 (2012), arXiv:1103.0543.

[33] P. A. M. Dirac, *Proc. Roy. Soc. Lond. A* **167**, 148 (1938).

[34] B. S. DeWitt and R. W. Brehme, *Annals Phys.* **9**, 220 (1960).

[35] C. R. Galley and B. L. Hu, *Phys. Rev. D* **79**, 064002 (2009), arXiv:0801.0900 [gr-qc].

[36] R. A. Porto, *Phys. Rept.* **633**, 1 (2016), arXiv:1601.04914 [hep-th].

[37] A. Pound, *Phys. Rev. Lett.* **109**, 051101 (2012), arXiv:1201.5089.

[38] S. E. Gralla, *Phys. Rev. D* **85**, 124011 (2012), arXiv:1203.3189.

[39] S. Detweiler, *Phys. Rev. D* **85**, 044048 (2012), arXiv:1107.2098.

[40] A. Pound and J. Miller, *Phys. Rev. D* **89**, 104020 (2014), arXiv:1403.1843 [gr-qc].

[41] A. Pound, *Phys. Rev. D* **90**, 084039 (2014), arXiv:1404.1543 [gr-qc].

[42] A. Pound, *Phys. Rev. D* **92**, 104047 (2015), arXiv:1510.05172 [gr-qc].

[43] M. van de Meent and A. G. Shah, *Phys. Rev. D* **92**, 064025 (2015), arXiv:1506.04755 [gr-qc].

[44] M. van de Meent, (2016), arXiv:1606.06297 [gr-qc].

[45] N. K. Johnson-McDaniel, *Phys. Rev. D* **90**, 024043 (2014), arXiv:1405.1572 [gr-qc].

[46] A. G. Shah, *Phys. Rev. D* **90**, 044025 (2014), arXiv:1403.2697 [gr-qc].

[47] N. Sago, R. Fujita, and H. Nakano, *Phys. Rev. D* **93**, 104023 (2016), arXiv:1601.02174 [gr-qc].

[48] K. S. Thorne and J. B. Hartle, *Phys. Rev. D* **31**, 1815 (1984).

[49] S. L. Detweiler, *Class. Quant. Grav.* **22**, S681 (2005), arXiv:gr-qc/0501004 [gr-qc].

[50] S. E. Gralla and R. M. Wald, *Class. Quant. Grav.* **25**, 205009 (2008), [Erratum: *Class. Quant. Grav.* 28, 159501 (2011)], arXiv:0806.3293 [gr-qc].

[51] S. L. Detweiler, *Phys. Rev. D* **77**, 124026 (2008), arXiv:0804.3529.

[52] N. Sago, L. Barack, and S. L. Detweiler, *Phys. Rev. D* **78**, 124024 (2008), arXiv:0810.2530.

[53] A. Le Tiec, *Int. J. Mod. Phys. D* **23**, 1430022 (2014), arXiv:1408.5505.

[54] A. G. Shah, T. S. Keidl, J. L. Friedman, D.-H. Kim, and L. R. Price, *Phys. Rev. D* **83**, 064018 (2011), arXiv:1009.4876 [gr-qc].

[55] A. G. Shah, J. L. Friedman, and B. F. Whiting, *Phys. Rev. D* **89**, 064042 (2014), arXiv:1312.1952 [gr-qc].

[56] L. Blanchet, S. L. Detweiler, A. Le Tiec, and B. F. Whiting, *Phys. Rev. D* **81**, 064004 (2010), arXiv:0910.0207 [gr-qc].

[57] L. Blanchet, S. L. Detweiler, A. Le Tiec, and B. F. Whiting, *Phys. Rev. D* **81**, 084033 (2010), arXiv:1002.0726.

[58] L. Blanchet, G. Faye, and B. F. Whiting, *Phys. Rev. D* **89**, 064026 (2014), arXiv:1312.2975 [gr-qc].

[59] A. Zimmerman, A. G. M. Lewis, and H. P. Pfeiffer, (2016), arXiv:1606.08056 [gr-qc].

[60] A. Le Tiec, L. Blanchet, and B. F. Whiting, *Phys. Rev. D* **85**, 064039 (2012), arXiv:1111.5378 [gr-qc].

[61] L. Blanchet, A. Buonanno, and A. Le Tiec, *Phys. Rev. D* **87**, 024030 (2013), arXiv:1211.1060 [gr-qc].

[62] A. Le Tiec, *Phys. Rev. D* **92**, 084021 (2015), arXiv:1506.05648 [gr-qc].

[63] T. Damour, *Phys. Rev. D* **81**, 024017 (2010), arXiv:0910.5533.

[64] L. Barack, T. Damour, and N. Sago, *Phys. Rev. D* **82**, 084036 (2010), arXiv:1008.0935 [gr-qc].

[65] S. Akcay, L. Barack, T. Damour, and N. Sago, *Phys. Rev. D* **86**, 104041 (2012), arXiv:1209.0964 [gr-qc].

[66] S. Akcay and M. van de Meent, *Phys. Rev. D* **93**, 064063 (2016), arXiv:1512.03392 [gr-qc].

[67] A. Le Tiec, E. Barausse, and A. Buonanno, *Phys. Rev. Lett.* **108**, 131103 (2012), arXiv:1111.5609 [gr-qc].

[68] L. Barack and N. Sago, *Phys. Rev. Lett.* **102**, 191101 (2009), arXiv:0902.0573.

[69] L. Barack and N. Sago, *Phys. Rev. D* **83**, 084023 (2011), arXiv:1101.3331.

[70] A. Le Tiec, A. H. Mroue, L. Barack, A. Buonanno, H. P. Pfeiffer, N. Sago, and A. Taracchini, *Phys. Rev. Lett.* **107**, 141101 (2011), arXiv:1106.3278 [gr-qc].

[71] S. R. Dolan, N. Warburton, A. I. Harte, A. Le Tiec, B. Wardell, and L. Barack, *Phys. Rev. D* **89**, 064011 (2014), arXiv:1312.0775 [gr-qc].

[72] D. Bini and T. Damour, *Phys. Rev. D* **90**, 024039 (2014), arXiv:1404.2747.

[73] S. R. Dolan, P. Nolan, A. C. Ottewill, N. Warburton, and B. Wardell, *Phys. Rev. D* **91**, 023009 (2015), arXiv:1406.4890.

[74] D. Bini and T. Damour, *Phys. Rev. D* **91**, 064064 (2015), arXiv:1503.01272.

[75] A. G. Shah and A. Pound, *Phys. Rev. D* **91**, 124022 (2015), arXiv:1503.02414 [gr-qc].

- [76] D. Bini and T. Damour, *Phys. Rev. D* **90**, 124037 (2014), arXiv:1409.6933.
- [77] D. Bini and A. Geralico, *Phys. Rev. D* **91**, 084012 (2015).
- [78] P. Nolan, C. Kavanagh, S. R. Dolan, A. C. Ottewill, N. Warburton, and B. Wardell, *Phys. Rev. D* **92**, 123008 (2015), arXiv:1505.04447 [gr-qc].
- [79] D. Bini and T. Damour, *Phys. Rev. D* **91**, 064050 (2015), arXiv:1502.02450 [gr-qc].
- [80] N. K. Johnson-McDaniel, A. G. Shah, and B. F. Whiting, *Phys. Rev. D* **92**, 044007 (2015), arXiv:1503.02638.
- [81] C. Kavanagh, A. C. Ottewill, and B. Wardell, *Phys. Rev. D* **92**, 084025 (2015), arXiv:1503.02334.
- [82] A. G. Shah, J. L. Friedman, and T. S. Keidl, *Phys. Rev. D* **86**, 084059 (2012), arXiv:1207.5595.
- [83] C. Kavanagh, A. C. Ottewill, and B. Wardell, *Phys. Rev. D* **93**, 124038 (2016), arXiv:1601.03394 [gr-qc].
- [84] S. Isoyama, L. Barack, S. R. Dolan, A. Le Tiec, H. Nakano, *et al.*, *Phys. Rev. Lett.* **113**, 161101 (2014), arXiv:1404.6133.
- [85] A. Le Tiec *et al.*, *Phys. Rev. D* **88**, 124027 (2013), arXiv:1309.0541 [gr-qc].
- [86] S. Akcay, A. Le Tiec, L. Barack, N. Sago, and N. Warburton, *Phys. Rev. D* **91**, 124014 (2015), arXiv:1503.01374 [gr-qc].
- [87] S. Hopper, C. Kavanagh, and A. C. Ottewill, *Phys. Rev. D* **93**, 044010 (2016), arXiv:1512.01556 [gr-qc].
- [88] D. Bini, T. Damour, and A. Geralico, *Phys. Rev. D* **93**, 064023 (2016), arXiv:1511.04533 [gr-qc].
- [89] D. Bini, T. Damour, and A. Geralico, *Phys. Rev. D* **93**, 104017 (2016), arXiv:1601.02988 [gr-qc].
- [90] D. Bini, T. Damour, and A. Geralico, *Phys. Rev. D* **93**, 124058 (2016), arXiv:1602.08282 [gr-qc].
- [91] J. Steinhoff, T. Hinderer, A. Buonanno, and A. Taracchini, (2016), arXiv:1608.01907 [gr-qc].
- [92] T. Damour, P. Jaranowski, and G. Schaefer, *Phys. Rev. D* **77**, 064032 (2008), arXiv:0711.1048 [gr-qc].
- [93] J. Hartung, J. Steinhoff, and G. Schaefer, *Annalen Phys.* **525**, 359 (2013), arXiv:1302.6723 [gr-qc].
- [94] J. Hartung and J. Steinhoff, *Annalen Phys.* **523**, 783 (2011), arXiv:1104.3079 [gr-qc].
- [95] B. Carter, *Phys. Rev.* **174**, 1559 (1968).
- [96] R. Penrose, *Annals N. Y. Acad. Sci.* **224**, 125 (1973).
- [97] J.-A. Marck, *Proceedings of the Royal Society of London. A. Mathematical and Physical Sciences* **385**, 431 (1983).
- [98] D. Bini, A. Geralico, and R. T. Jantzen, (2016), arXiv:1607.08427 [gr-qc].
- [99] M. Mathisson, *Acta Phys. Polon.* **6**, 163 (1937).
- [100] A. Papapetrou, *Proc. Roy. Soc. Lond.* **A209**, 248 (1951).
- [101] S. Akcay, N. Warburton, and L. Barack, *Phys. Rev. D* **88**, 104009 (2013), arXiv:1308.5223 [gr-qc].
- [102] L. Barack, A. Ori, and N. Sago, *Phys. Rev. D* **78**, 084021 (2008), arXiv:0808.2315 [gr-qc].
- [103] N. Warburton, S. Akcay, L. Barack, J. R. Gair, and N. Sago, *Phys. Rev. D* **85**, 061501 (2012), arXiv:1111.6908 [gr-qc].
- [104] L. Barack and N. Sago, *Phys. Rev. D* **75**, 064021 (2007), arXiv:gr-qc/0701069 [gr-qc].
- [105] B. Wardell, personal communication (June 2016).
- [106] L. Barack and A. Ori, *Phys. Rev. D* **61**, 061502 (2000), arXiv:gr-qc/9912010 [gr-qc].
- [107] B. Wardell, *Green Functions and Radiation Reaction From a Spacetime Perspective*, Ph.D. thesis, University Coll., Dublin, CASL (2009), arXiv:0910.2634 [gr-qc].
- [108] A. Heffernan, A. Ottewill, and B. Wardell, *Phys. Rev. D* **86**, 104023 (2012), arXiv:1204.0794 [gr-qc].
- [109] N. Warburton and B. Wardell, *Phys. Rev. D* **89**, 044046 (2014), arXiv:1311.3104 [gr-qc].
- [110] A. Bohe, S. Marsat, G. Faye, and L. Blanchet, *Class. Quant. Grav.* **30**, 075017 (2013), arXiv:1212.5520.
- [111] T. Damour and N. Deruelle, *Ann. Inst. Henri Poincaré* **43**, 107 (1985).
- [112] R.-M. Memmesheimer, A. Gopakumar, and G. Schäfer, *Phys. Rev. D* **70**, 104011 (2004), arXiv:gr-qc/0407049.
- [113] K. G. Arun, L. Blanchet, B. R. Iyer, and M. S. S. Qusailah, *Phys. Rev. D* **77**, 064035 (2008), arXiv:0711.0302 [gr-qc].
- [114] L. Blanchet and B. R. Iyer, *Class. Quant. Grav.* **20**, 755 (2003), arXiv:gr-qc/0209089 [gr-qc].
- [115] A. Le Tiec, personal communication (July 2016).
- [116] S. Hopper, personal communication (March 2016).
- [117] S. Mano, H. Suzuki, and E. Takasugi, *Prog. Theor. Phys.* **95**, 1079 (1996), arXiv:gr-qc/9603020 [gr-qc].

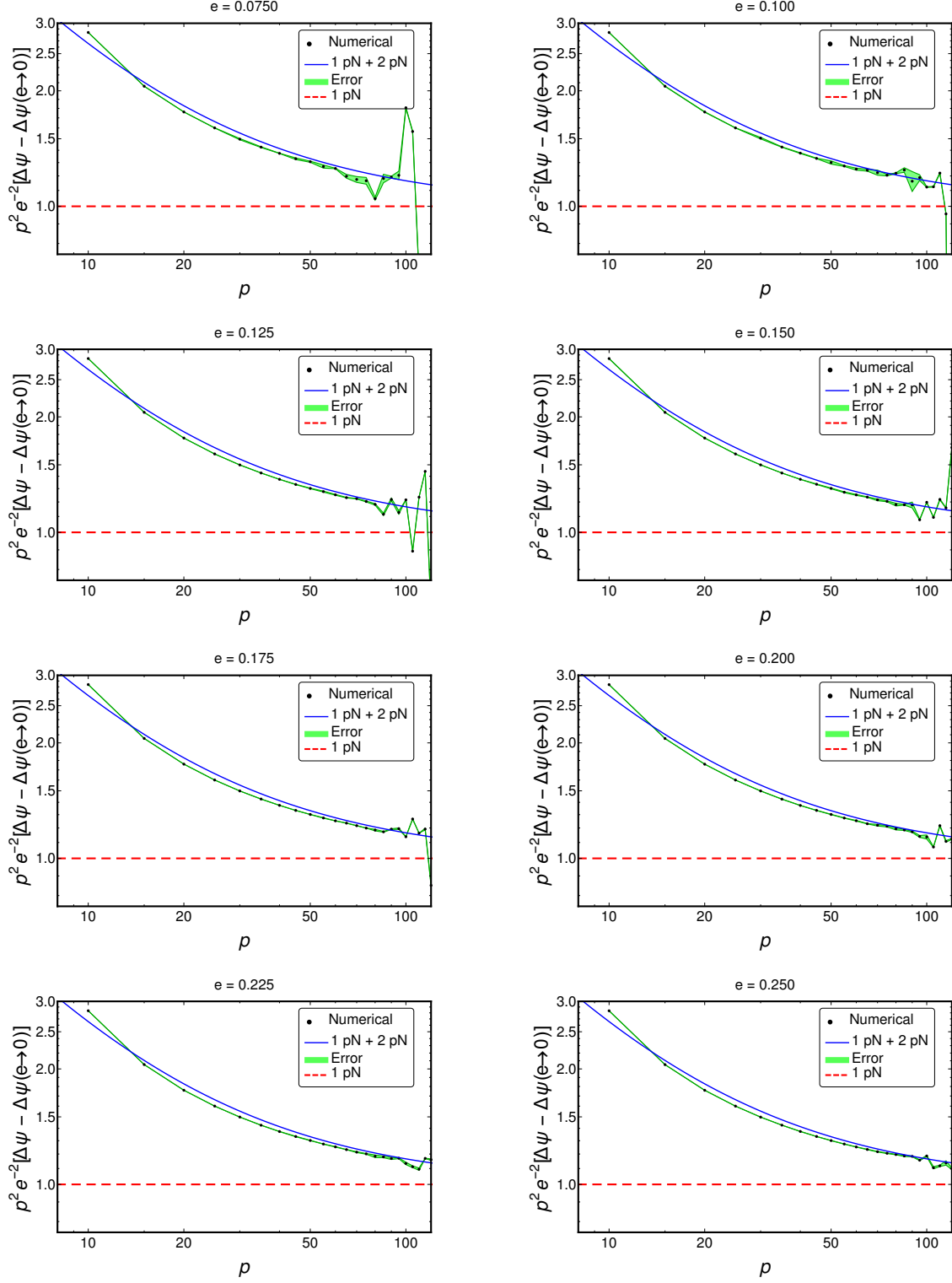


FIG. 3. Numerical extraction of the $\mathcal{O}(e^2)$ terms plotted — after being multiplied by p^2 — for $e = \{0.075, 0.1, 0.125, \dots, 0.225, 0.25\}$. From our post-Newtonian derivation, we know that this term equals $\left[1 + \left(\frac{341}{16} - \frac{123\pi^2}{256}\right) \frac{1}{p}\right]$ shown by the solid blue curves. The numerical residual represented by the black dots contains contributions from the unknown $\mathcal{O}(p^{\leq -4} e^{\geq 4})$ terms which is why the solid blue curves are shifted away from the black dots. The red dashed lines mark the 1 pN term e^2/p^2 . The green strips are our estimated numerical errors. As we explain in the text, our data is noisier for low eccentricities and high p values where the absolute magnitude of the term that we extract from the numerical data decreases. Note that although we calculate the errors only at the p values given in Table II we have connected the error bars in the plots with green shaded curves for visualization purposes.

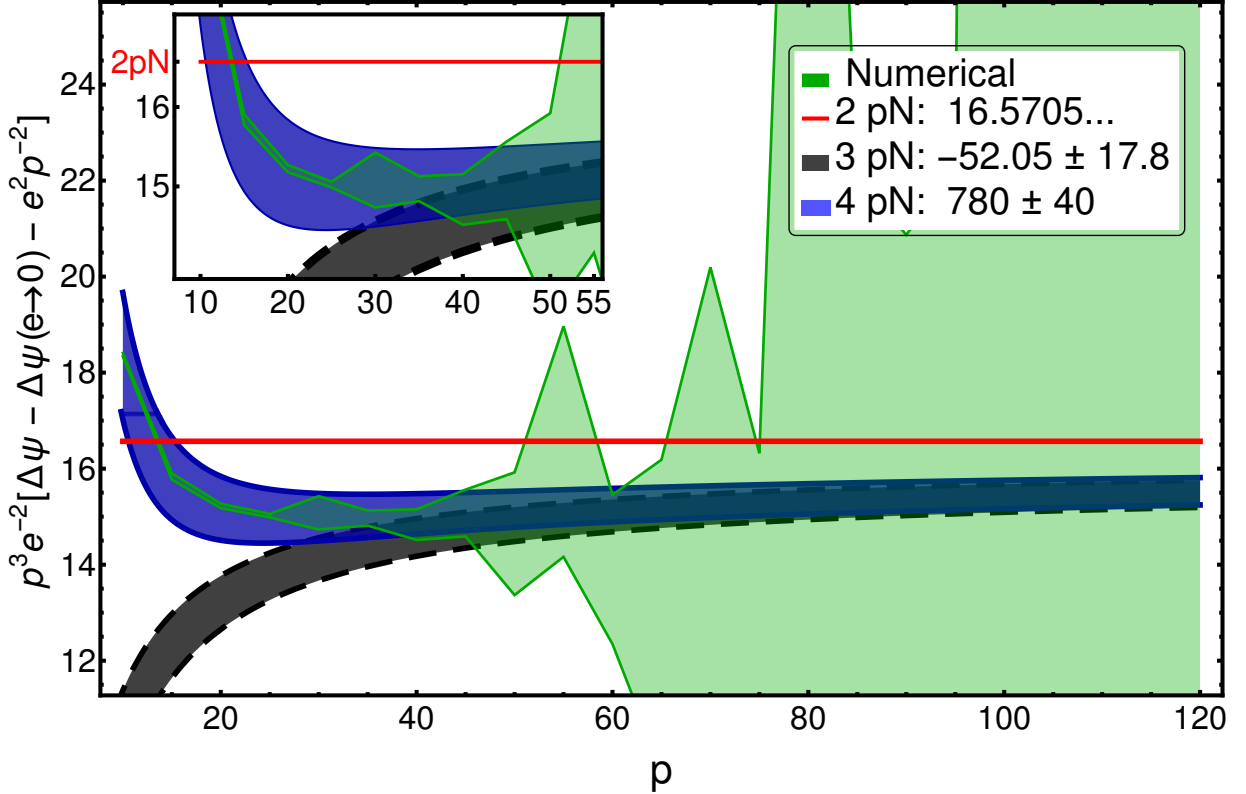


FIG. 4. Numerical extraction of the subdominant $\mathcal{O}(e^2/p^3)$, $\mathcal{O}(e^2/p^4)$, $\mathcal{O}(e^2/p^5)$ terms from all our data. Our pN derivation yields $\left(\frac{341}{16} - \frac{123\pi^2}{256}\right) \approx 16.5705$ for the coefficient of the $\mathcal{O}(e^2/p^3)$ term which we plot as the thick red line. The numerical residual $p^3 e^{-2} [\Delta\psi - \lim_{e \rightarrow 0} \Delta\psi]$ is represented by the green shaded error region. Since our error grows with increasing p our data is only ‘clean’ for $10 \leq p \lesssim 45$ where we can estimate the coefficients of the $\mathcal{O}(e^2/p^4)$, $\mathcal{O}(e^2/p^5)$ terms. The black region between the dashed, black curves is our estimation for the coefficient of the $\mathcal{O}(e^2/p^4)$ term and the blue region between the solid, blue curves for the coefficient of the $\mathcal{O}(e^2/p^5)$ term. Our error region grows rather large for $p \gtrsim 45$ mostly because of our low-eccentricity data where the absolute magnitude of this term is comparable to our error.